8-22-2018

Numerical Simulation of High Energy Laser Propagation

Dana F. Morrill

AFIT/ENC Dissertation:
Numerical Simulation of High Energy Laser Propagation

DISSERTATION

Dana F. Morrill, Maj, USAF

AFIT-ENC-DS-18-S-003

DEPARTMENT OF THE AIR FORCE
AIR UNIVERSITY

AIR FORCE INSTITUTE OF TECHNOLOGY

Wright-Patterson Air Force Base, Ohio

AFIT-ENC-DS-18-S-003

AFIT/ENC DISSERTATION:
NUMERICAL SIMULATION OF HIGH ENERGY LASER PROPAGATION

DISSERTATION

Presented to the Faculty

Graduate School of Engineering and Management

Air Force Institute of Technology

Air University

Air Education and Training Command

in Partial Fulfillment of the Requirements for the

Degree of Doctor of Philosophy in Applied Mathematics

Dana F. Morrill, B.S., M.S.

Maj, USAF

August 20, 2018

AFIT-ENC-DS-18-S-003

AFIT/ENC DISSERTATION:

NUMERICAL SIMULATION OF HIGH ENERGY LASER PROPAGATION

DISSERTATION

Dana F. Morrill, B.S., M.S.
Maj, USAF

Committee Membership:

Dr. Benjamin Akers
Chair

Dr. Steven Fiorino
Member

Maj Jonah Reeger, PhD
Member

Capt Richard Uber, PhD
Member

AFIT-ENC-DS-18-S-003

Abstract

High energy lasers have many applications, such as in aerospace, weapons, wireless power transfer, and manufacturing. Fluid-laser interaction is important to predicting power at receiver, and other measures of laser beam quality. Typically the carrying medium of the laser is modeled statistically. This dissertation describes a novel method of coupling fluid dynamics to beam propagation in free space. The coupled laser-fluid solver captures dynamic interaction of fluid temperature and beam intensity. Ultimately, the model captures the effects of fluid convection in the laser intensity-field.

Boundary conditions play an important role for fluid dynamics, more so than for beam dynamics. Simulation convergence and time performance are compared for three fluid boundary conditions: periodic boundary conditions, finite box domain, and an open boundary condition.

Scintillation is included in the final simulations. Scintillation is an important factor in laser beam quality. It is usually incorporated via phase-screens on the beam alone. A unique hybrid volumetric phase-screen model is developed to simulate laser-fluid interaction in the presence of small turbulence. The hybrid model is simulated and results of simulations, where scintillation is asymptotically incorporated into the coupled fluid-beam simulation, are presented.

Table of Contents

Page

List of Figures

Figure Page

AFIT/ENC DISSERTATION:

NUMERICAL SIMULATION OF HIGH ENERGY LASER PROPAGATION

I. Introduction

A study of the atmospheric effects on high energy laser (HEL) propagation through the atmosphere was made with emphasis on the dynamic interaction between the heat generated by the laser beam and the resulting change in refractive index. Laser heating of the medium induces convection in the fluid carrying the laser beam. In turn, the fluid heating alters the index of refraction, bending the laser beam away from the heated region [3] as well as deforming the beam spot.

Thermal blooming occurs when a laser beam propagates through an absorbing medium. The energy that is absorbed by the medium is generally very small, but the effect is to heat the medium, giving rise to local gradients in the density and temperature of the medium. The refractive index of the medium changes in the immediate vicinity of the beam where the heating is greatest; The beam becomes defocused and spreads - as denoted by "blooming" [1].

Thermal blooming has been discussed since lasers first became powerful enough to noticeably heat a medium in 1964 [4] and has been well documented since its first observance [5]. Thermal blooming's relevance to laser propagation grows in proportion to laser power.

It is clear from an overview of laser history that lasers are growing more and more powerful [6, 7, 8]. Continuous wave HEL's producing kilowatt levels of power are commonplace in fabrication applications and medical surgery, and megawatt lasers are being studied for application in rock drilling [9]. With increased laser power come

more applications. These include, but are not limited to, remote sensing of clouds for ice-crystal content [10], airborne laser scanning for range and object identification [11], targeting [6], radio astronomy, space radio communication, and satellite communication [1].

NASA is developing HEL-based power beaming system to enable wireless power transfer [12]. Contactless energy transfer over long distances (km range) using 1-100 W lasers also has application in unmanned aerial systems [13, 12]. Such systems integrate remote laser communications and lasers used to remotely recharge batteries in the network [14].

In all of the applications mentioned beam quality is of concern. Thermal blooming is a negative effect on beam quality and amount of power delivered to an end source. Many of these applications have aroused the interest of Department of Defense and government agencies who require measures of merit in order to discuss feasibility of its systems acquisition [6, 15]. Regardless of the measure of merit selected, understanding thermal blooming and being able to predict and characterize HEL beam propagation through a medium is necessary.

An important application of this research is to provide a computational solution to HEL propagation that fully incorporates both fluid and light flows, and their interactions. This can serve as a wide benchmark for computationally fast operational propagation simulations.

This dissertation develops a novel method for numerically modeling laser induced convection in its carrying medium is developed. Beam propagation is simulated volumetrically with FFT methods using interpolation between two-dimensional transverse temperature instances. Fluid dynamics are simulated with a predictor-corrector scheme, the Boussinesq model uses beam intensity from the Paraxial simulation to force temperature.

Boundary conditions for the free space problem are examined. The boundary conditions study in this dissertation provides a novel analysis of FOB. FOB provides an accurate, if costly, method for modeling laser propagation in an open environment. Imposing periodic boundary conditions is not as accurate, but access to FFT gives advantages in computation costs and allows for increased resolution in a reasonable amount of time.

Scintillation is included in the coupled solver using a hybrid volumetric and phase-screen method. This is a computationally tractable method that allows inclusion of scintillation initially present in the media as well as dynamics. Asymptotically incorporating scintillation on intensity will be shown to create distortion in the beam intensity. Behavior of the coupled solver is shown to parallel behavior of a laser experiment photographed by Wick and Lloyd.

This disertation's structure is as follows, the remainder of this chapter covers some of the relevant work that has been done with respect to thermal blooming, including the literature on thermal blooming and numerical models used to describe laser induced convection. Chapter II discusses simulation assumptions and the fluid and beam models in depth to describe how they fit into the numerical simulation of laser-fluid interaction. Chapter III describes the numerical method applied for the coupled laser-fluid simulation. Chapter IV covers a boundary conditions study comparing periodic boundary conditions, finite box boundary conditions, and an open boundary condition method described by Fornberg in [16]. Chapter V lays out the choices made in the scintillated coupled laser-fluid simulation. Finally Chapter VI presents the conclusions of this study as well as future work.

1.1 Thermal Blooming

This section discusses the theory and literature dealing with thermal blooming. Past work is described along with a discussion of this study's contributions.

Thermal blooming depends on several factors including (1) laser-beam characteristics like wavelength, phase and irradiance (2) kinetics of absorption, i.e. time for absorbed energy to heat the medium, (3) mode of heat transfer balancing the absorbed energy (4) time-scale and (5) propagation medium and scenario - such as path length, optical properties, platform speed, slewing and so forth [3, 1]. The coupled laser-fluid model utilizes the convective time-scale, incorporating the effects of gravity. The coupled model numerically simulates the effect of convective motion of the heated atmosphere on the propagation of the laser seen in beam bending and spot deformation.

Initial efforts centered on stationary continuous wave beams in a fluid where thermal conduction dominated as the primary heat transfer mechanism, the effect observed and modeled was essentially a uniformly spread beam at the end sensor. These efforts assume a uniform, quiescent medium with no self-induced convection due to heating from the HEL beam, resulting in a beam that spread radially with defocused intensity as the beam passed through the media [3, 17, 18].

By 1969 interest shifted to considering a medium in motion [3]. These models assume a uniform wind moving across the beam path as it passes through an atmosphere [5, 19, 20, 21, 22, 23]. Further efforts focused on changing the atmosphere through which the beam might pass [4, 23, 24, 25], but prescribed the atmosphere as a static, statistical description.

It is not tenable to directly simulate atmospheric turbulence at the scale of laser wavelengths. Typically an envelope equation is applied with discretely placed phase screens where the small-scale fluctuations in the atmosphere are described statistically

[26, 27, 28, 29, 30, 31].

Phase screens are $N \times N$ arrays of random complex numbers with statistics matching those described by a spatial power spectral density function of refractive index fluctuations, $\Phi_n(\kappa)$, where κ is the spatial wave number [1, 30]. Several options are available for selecting $\Phi_n(\kappa)$ [1, 29, 30, 31]; variance of the distribution of turbulence can be expressed

$$\sigma^2(\kappa) = \left(\frac{2\pi}{N\Delta z}\right)^2 \Phi(\kappa),$$

where $\Phi(\kappa) = 2\pi\|\kappa\|^2 \Delta z \Phi_n(\kappa)$ and Δz is the space between phase screens, which is then used to define a phase screen in x-space

$$\phi(x, y) = \widetilde{C\sigma(\kappa)} \tag{1}$$

where C is a random $N \times N$ array drawn from a distribution with zero mean and variance equal to one. This method provides two independent phase screens in real and imaginary parts of (1) which can be convolved with the envelope equation [30, 31], or the statistics of the temperature field [25, 32], to get the expected intensity.

Φ_n is usually computed by relying on the refractive index structure parameter, C_n^2, a scalar amplitude of refractive index fluctuations within the inner and outer scales of turbulence measure [1]. In describing turbulence, and therefore scintillation, we rely on C_n^2 to derive the statistics of turbulence. In [33, 34], Pries gives a discussion of measured C_n^2 at White Sands Missile Range over a 2 week period, and summarizes Gebhardt's description of strong turbulence in terms of the structure parameter: $C_n^2 \geq 10^{-14} m^{-2/3}$ [35].

In [36] Fiorino et al put C_n^2 in terms of the temperature structure parameter, C_T^2, with

$$C_n^2 = C_T^2 \left[79 \times 10^{-6} \frac{P}{T^2}\right]^2, \tag{2}$$

where P is the pressure and T is the temperature. Thus C_n^2 can be computed with C_T^2, which in turn is gathered by measurement of temperature values via thermosonde [36]. In [37] Rohmistrov et al compute the temperature structure constant using

$$C_T^2 = \langle [T'(t + \Delta t) - T'(t)]^2 \rangle (\langle V \rangle \Delta t)^{-2/3}, \tag{3}$$

where $\langle V \rangle$ is the absolute value of wind velocity mean vector defined by $\langle V \rangle = \sqrt{\langle u \rangle^2 + \langle v \rangle^2}$ and $T' = T - \langle T \rangle$. For a discrete samples, f_k, of a function $f(t)$ averages are computed with the equation $\langle f \rangle = \frac{1}{N} \sum_{k=0}^{N-1} f_k$, where N is the number of samples. This simulates how an ultrasonic anemometer computes C_T^2 [37].

Difficulty in getting accurate C_n^2 measurement [38], alternatively, can be overcome by using the implicit dependence of the structure function on propagation distance, z, to compute atmospheric coherence diameter, r_0 [39]. The method described in Chapter V opts to employ spatial coherence radius, r_0, to compute the phase screen.

A hybrid approach is employed computing fluid dynamics volumetrically to simulate the dynamics of self-induced convection in the presence of turbulence, using phase spectrum density to generate a temperature phase screen to model turbulent atmosphere. The next section covers the literature for the optical fluid solver.

1.2 Fluid Dynamics

The Navier-Stokes equations govern physical deformations of a Newtonian fluid, so we use it to model the dynamics induced by a laser propagated through a medium. The Navier-Stokes equation as given by Tritton in [40] is:

$$\rho \frac{D\mathbf{u}}{Dt} = -\nabla p + \mu \nabla^2 \mathbf{u} + \mathbf{F}, \tag{4}$$

where $\mathbf{u}$ is the velocity vector, ρ is the density of the medium, μ is the coefficient of viscosity and $\mathbf{F}$ represents the contributions of other forces contributing to the specification of the problem. Using the standard notation for convective derivatives:

$$\frac{Df}{Dt} = f_t + (f \cdot \nabla)f$$

for any time-dependent function f.

Chorin, in [41], applies the Boussinesq approximation to simplify Navier-Stokes equations in order to solve a thermal convection problem. The thermal convection problem uses the Boussinesq approximation, since it is solved immediately about the laser spot.

The Boussinesq approximation ignores density variations except where it is influenced by acceleration due to gravity. Sound waves are neglected under application of the Boussinesq approximation since sound waves move via density variations. The advantage is that the problem is greatly simplified [40]. Moreover the turbulence we are modeling is largely due to refractive index fluctuations in the medium. In electromagnetic wave propagation refractive index fluctuations are caused almost entirely by variations in temperature; pressure variations are relatively small and rapidly dispersed [42, 43]. So while the Boussinesq is a simplification of fluid dynamics we are justified in applying it in our application.

Having discussed the reasoning for choosing a Boussinesq fluid solver, the next section covers the the beam propagation model.

1.3 Beam Propagation

We follow Sprangle, Peñano, et al, in utilizing the Paraxial equation derived from Maxwell's equations [44, 45, 46]. Sprangle states the Paraxial equation, with energy

field $\tilde{E} = \mathrm{A}e^{-ik\eta z} + c.c.$ for $\eta = \eta_0 + \epsilon^2 k\eta_1$, as

$$\left(-\nabla^2 + 2ik\eta_0\frac{\partial}{\partial z} + 2\eta_0\eta_1 k^2\right)\mathrm{A} = 0 \tag{5}$$

where η is the index of refraction with η_0 the average index of refraction and η_1 a perturbation of refractive index, and k the wave number of the laser. ∇^2 is the Laplace operator in the transverse direction ($\nabla^2\mathrm{A} = \mathrm{A}_{xx} + \mathrm{A}_{yy}$) [46], applying notation modified from that used by Peñano and Sprangle. Following Sprangle et al, the expression includes terms to address effects of absorption and scattering in the atmosphere, β_a and β_s respectively:

$$\left(-\nabla^2 + 2ik\eta_0\frac{\partial}{\partial z} + 2\eta_0\eta_1 k^2 - \beta_a - \beta_s\right)\mathrm{A} = 0. \tag{6}$$

Having established the choice of the Paraxial equation, we move on to Chapter II which covers the numerical solution of these equations.

II. Assumptions and Derivatavations

Assumptions used in the optical fluid solver and the simulation of laser propagation through a medium are presented in this chapter. A derivation of the Boussinesq equations is then provided followed by a discussion of the numerical methods used to approximate a solution. The Paraxial equation is then derived followed by a discussion of index of refraction. The chapter is concluded with a presentation of the numerical methods used to simulate laser propagation.

2.1 Assumptions

1. Incompressible flow: it is assumed that $\nabla \cdot \mathbf{u} = 0$. Pressure variations in the medium do not significantly affect density variations. This allows for the Boussinesq approximation.

2. Isobaric heating: A long distance beam length is assumed, which further implies that the characteristic pulse length, t_p, must be much larger than the time it takes for the beam to propagate through the beam channel, $t_{ac} = R_0/c$; R_0 is the beam radius. Therefore (8) can be applied since pressure equalizes quickly, and changes in gas density are linearly related to changes in temperature [47].

3. Quiescent initial conditions: The primary turbulence is that which is induced by the beam itself. This allows for the laser beam induced fluid dynamics to be "seen". Similarly, a high power laser is assumed: it is required that the laser have sufficient power to ensure that heating from the beam dominates any scintillation arising from turbulence. Essentially this requires a high contrast between the initial turbulence and the turbulence induced by the laser.

2.2 Boussinesq Equations

Following the discussion of Boussinesq fluid equations in [40], it is assumed that the effect of the laser on the atmosphere is not large, allowing for the Boussinesq approximation for the fluid flow. This assumption allows all but the temperature variations to be ignored. Variations to density are included only inasmuch as they relate to variations in temperature.

We consider incompressible fluid flows,

$$\nabla \cdot \mathbf{u} = 0. \tag{7}$$

$\rho D\mathbf{u}/Dt$ is placed with $\rho_0 D\mathbf{u}/Dt$ in equation (4), where ρ_0 is the average density and is constant. Setting

$$\mathbf{F} = \rho\mathbf{g}$$

allows for the effect of gravity. Density variations may be important, so density is defined $\rho = \rho_0 + \delta\rho$. Gravitational acceleration can be written as $g = \nabla\Phi$, where Φ is a potential and can be expressed as $\mathbf{g} = g\hat{z}$ and $\Phi = gz$ if z is taken to be vertically downwards. Thus

$$\mathbf{F} = (\rho_0 + \delta\rho)\nabla\Phi = \nabla(\rho_0\Phi) + \delta\rho\mathbf{g}.$$

Setting $P = p = \rho_0\Phi$ equation (4) gives

$$\rho_0 \frac{D\mathbf{u}}{Dt} = \nabla P + \mu\nabla^2\mathbf{u} + \delta\rho\mathbf{g} \tag{8}$$

Considering the influence of temperature variations, we have to assume $\delta\rho \neq 0$. As part of the Boussinesq approximation, though, the dependence of ρ on T is linearized

$$(\rho_1 - \rho_0) = \alpha\rho_0(T_1 - T_0),$$

which can be written

$$\delta\rho = \alpha\rho_0\delta T,$$

where α is the coefficient of fluid expansion (for ideal gasses $\alpha = 1/T$). Exploiting the assumption of linearity between density and temperature write

$$\delta\rho = \rho_0\frac{T}{T_0}\mathbf{e}_2.$$

Where T is now the temperature fluctuation (we derive equations in the fluctuations of T below) and T_0 is the reference temperature, and the vertical downward orientation of this forcing is denoted by the unit vector $\mathbf{e}_2 = [0, 1, 0]'$. This gives the Boussinesq dynamical equation

$$\frac{D\mathbf{u}}{Dt} = \frac{1}{\rho_0}\nabla P + \mu\nabla^2\mathbf{u} + \frac{g}{T_0}T\mathbf{e}_2. \tag{9}$$

It is assumed, in keeping with the Boussinesq approximation, that the fluid has a constant heat capacity per unit volume ρC_p. Thus $\rho C_p DT/Dt$ is the rate of heating per unit volume of a fluid particle. Heating is caused by transfer of heat from particle to neighboring particle by thermal conduction, and sometimes by internal heat generation. These terms in the heating equation correspond to viscosity and body force terms in equation (9). The conductive heat flux is

$$\mathbf{H} = -k\nabla T,$$

where k is the thermal conductivity of the fluid. Thus

$$\rho C_p\frac{DT}{Dt} = -\nabla\cdot\mathbf{H} + J \tag{10}$$

where J is the rate of internal heat generation per unit volume. Let k be constant

and equation (10) becomes

$$\frac{DT}{Dt} = \nu\nabla^2 T + \frac{J}{\rho C_P} \tag{11}$$

where $\nu = k/\rho C_p$ is the thermal diffusivity or kinematic viscosity. Moreover every term in which T appears is differentiated in space, so it is essentially an equation in terms of the fluctuation of T.

Drawing together (7), (9) and (11) gives the Boussinesq equations. Setting

$$\frac{J}{C_p\rho} = \beta_a|\mathrm{A}|^2,$$

where β_a is the coefficient for linear loss of energy due to atmospheric absorption and $|\mathrm{A}|^2$ is the intensity of the laser acting as our heat generation, expresses the Boussinesq equations as

$$\frac{D\mathbf{u}}{Dt} = \frac{1}{\rho_0}\nabla P + \mu\nabla^2\mathbf{u} + \frac{g}{T_0}T\mathbf{e}_2 \tag{12a}$$

$$\frac{DT}{Dt} = \nu\nabla^2 T + \frac{J}{\rho_0 C_p} = \nu\nabla^2 T + \beta_a|\mathrm{A}|^2 \tag{12b}$$

$$\nabla\cdot\mathbf{u} = 0. \tag{12c}$$

This method non-dimensionalizes (12) with velocity scale U, temperature scale T_0, and spatial length scale, L, in the transverse direction. The time scale is defined as $\tau = \frac{L}{U}$, and the pressure scale is defined as $P_0 = \rho_0 U^2$. We divide (12a) by $\dfrac{U^2}{L}$ on both sides, and divide both sides of (12b) by $\dfrac{UT_0}{L}$ to yield dimensionless parameters Re, Ri, Pe and St. This results in

$$\frac{D\mathbf{u}}{Dt} = \nabla P + \frac{1}{Re}\nabla^2\mathbf{u} + RiT\mathbf{e}_2 \tag{13a}$$

$$\frac{DT}{Dt} = \frac{1}{Pe}\nabla^2 T + St|\mathrm{A}|^2 \tag{13b}$$

$$\nabla \cdot \mathbf{u} = 0. \tag{13c}$$

where Re is the Reynolds number that describes inertia versus viscosity, Ri is the Richardson number describing velocity versus gravity wave speed, Pe is the Pèclet number which covers the thermal diffusion and St is the Stanton number describing the heating by the laser versus heat capacity of the medium. The formulae for these parameters are given mathematically by

$$Re = \frac{UL}{\mu}, \qquad Ri = \frac{U^2}{gL}, \qquad Pe = \frac{UL}{\nu}, \qquad St = \frac{A_0^2 \beta L}{UT_0}.$$

These constants are approached from the opposite direction than usual when discussing them. Instead of setting the values L, U et cetera, the values of Re, Ri, Pe and St are determined by the modeler. For each selected value for these constants there exists a continuum of scenarios of laser settings and atmospheric conditions that apply.

The next section discusses the numerical methods applied simulating the fluid dynamics of the problem.

Modeling the Boussinesq Equations.

The optical fluid model is numerically solved with a pressure correction method applied to both a fast Fourier solver and a finite difference solver.

In the finite difference solver the Boussinesq equations second order up-winding, as described by Shyy et al in [48], are employed to approximate the nonlinear terms

$$-(\mathbf{u} \cdot \nabla)\mathbf{u}, \text{ and } -(\mathbf{u} \cdot \nabla)T. \tag{14}$$

A centered difference scheme is used to approximate

$$\frac{1}{Re}\nabla^2\mathbf{u}, \text{ and } \frac{1}{Pe}\nabla^2 T. \tag{15}$$

A second order centered difference is applied so that the overall finite difference scheme has spatial convergence $O(h^2)$ for characteristic space step, h.

In the fast Fourier solver, nonlinear terms (14) and viscosity terms (15) are approximated in Fourier space. This gives the fast Fourier solver spectral spatial convergence [49].

To ensure that the divergence of the numerical fluid flow is zero, a pressure correction of divergence is included in both solvers. The divergence of (13a) is computed so that

$$\nabla^2 P = \nabla \cdot [(\mathbf{u} \cdot \nabla)\mathbf{u} - RiT\mathbf{e}_2]. \tag{16}$$

Equation (16) is a Poisson equation. In the finite difference solver, a second-order Poisson solver is used to update P and project off the divergence in (13a) [50, 51]. This "pressure correction" step ensures that $\nabla \cdot \mathbf{u} = 0$. The fast Fourier solver projects off divergence with the same process, but without a Poisson solver since P in (16) can be computed numerically in Fourier space.

Both the finite difference and Fourier solvers are combined with an RK-4 scheme over time to get $O(\Delta t^4)$ convergence in time. Convergence in time and space of the finite difference fluid solver, in terms of the fluid's divergence converging to zero, is discussed in the next section. Comparison of (13a) with temperature set equal to zero to Taylor-Green vortices, which have a known solution, is made in the next section as well.

Boussinesq Convergence.

Equation (13c) provides a valuable measure of merit for the finite difference fluid solver. This section provides an analysis of convergence of the fluid's divergence, as approximated by the finite difference solver, to zero as a function of time and space step sizes. A comparison of (13), with $Ri = 0$, is also made against the exact solution to Taylor-Green vortices, a special case of Navier-Stokes equations.

An $O(h^2)$, where h is the characteristic space step, numerical solver is combined with an $O(\Delta t^4)$ time-step scheme, where Δt is the time step, so that the finite difference solver's convergence to zero divergence, can be measured along two axes. Convergence to zero divergence is shown in Figure 1. Convergence of the finite difference solver as a function of step size, h, is shown on the left. Convergence as a function of time step size, Δt is shown on the right.

The left hand side of Figure 1 shows the finite difference solver has divergence converging to zero with slope two as h gets smaller. Similarly, the right hand side of Figure 1 shows the finite difference solver has divergence converging to zero with slope four as Δt gets smaller.

The value of Ri can be set to zero to get the standard Navier-Stokes equations. A special case of Navier-Stokes is Taylor-Green vortices, and this special case has a straight forward and closed form solution. Taylor-Green vortices are used to show that the Boussinesq equations are accurate, at least when they are not forced by temperature from an HEL propagating through the media.

The initial conditions for the problem are given by

$$\begin{aligned} u_0 &= A \cos ax \sin ay \\ v_0 &= B \sin bx \cos by, \end{aligned}$$

for $0 \leq x \leq 2\pi$, and $0 \leq y \leq 2\pi$, and $0 = Aa + Bb$ [52].

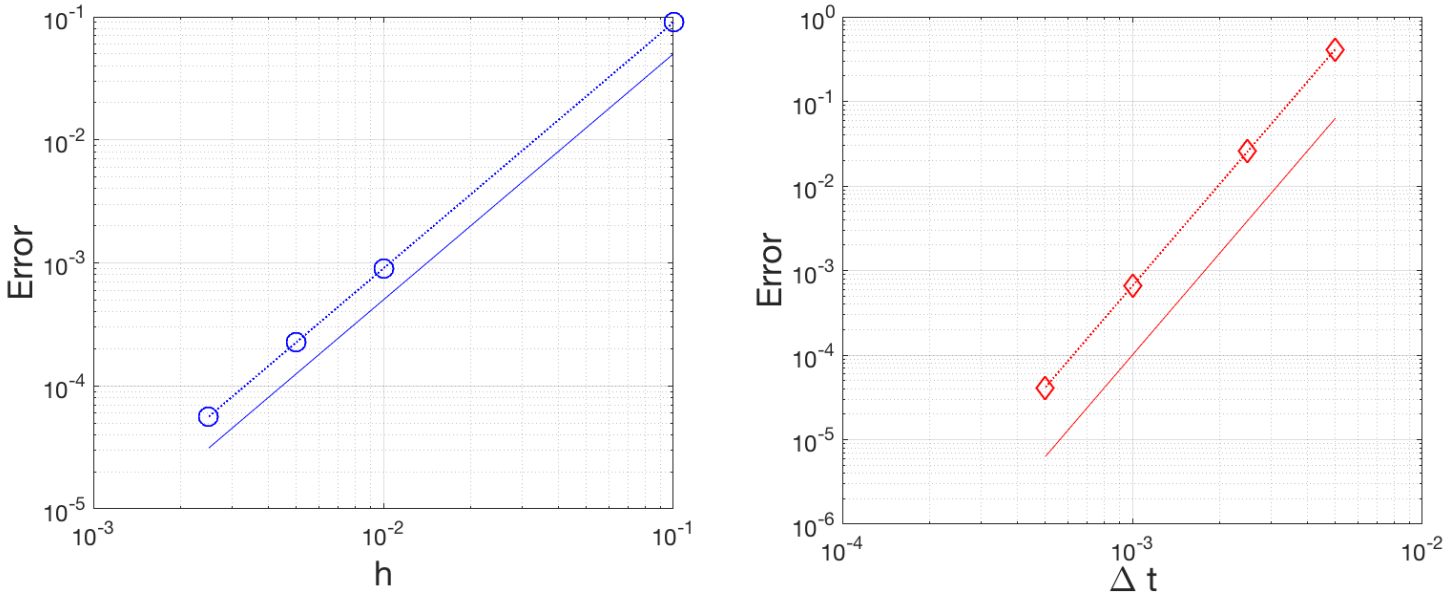

Figure 1. Left: plot of $\nabla \cdot \mathbf{u}$ against spatial step size; h represents the spatial step size in x and y. Right: Plot of $\nabla \cdot \mathbf{u}$ against time-step size; Δt represents the time step size. The y-axis is the divergence of the fluid flow as approximated with the finite difference solver. The divergence is shown to illustrate the convergence of the forced Boussinesq fluids solver. Divergence converging to zero is the equation $\nabla \cdot \mathbf{u} = 0$ converging to its true value at $O(h^2)$, since the incompressibility equation is explicitly tied to the other equations in the Boussinesq model (13), the system is converging at a rate $O(h^2)$ with respect to space step, and at a rate $O(\Delta t^4)$ with respect to time.

Using $A = a = b = 1$ and $B = -1$ provides the Taylor-Green vortex solution [52]:

$$\begin{aligned} u &= \cos x \sin y \mathrm{e}^{-2\nu t} \\ v &= -\sin x \cos y \mathrm{e}^{-2\nu t}. \end{aligned} \tag{17}$$

Equations (17) are used to check accuracy of the Boussinesq solver, of particular interest is the time-convergence of the un-forced Boussinesq. The plot of the errors are summarized in Figure 2.

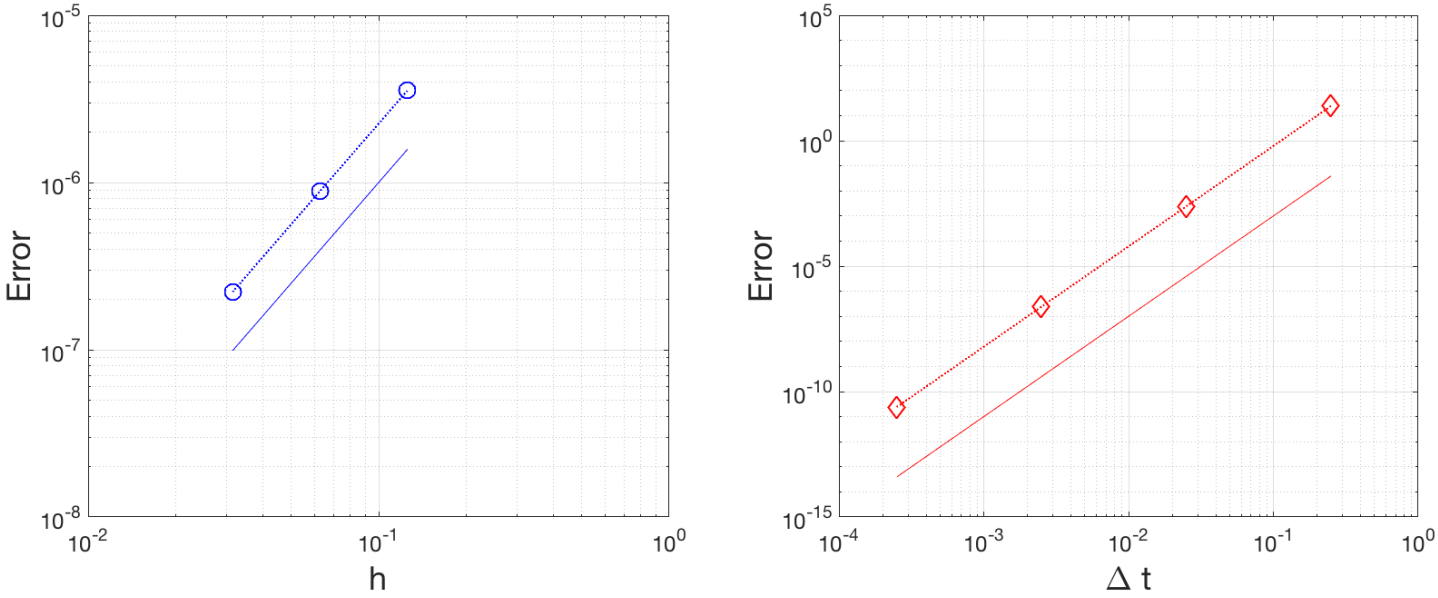

Figure 2. Error of Boussinesq equations without temperature forcing (setting the temperature forcing to zero and setting the initial conditions to satisfy the Taylor-Green vortex. Boussinesq is compared to Taylor-Green vortex. Left: The Boussinesq model converges to the true solution at $O(h^2)$; error follows along the $m = 2$ reference line showing the $O(h^2)$ convergence. Right: The Boussinesq model converges to the true solution at $O(\Delta t^4)$; error follows along the $m = 4$ reference line showing the $O(\Delta t^4)$ convergence. Error is $\|\mathbf{u}^* - \mathbf{u}\|_1$, the norm of the true value against the solved values.

2.3 Paraxial Equation

In this section the Paraxial equations are derived from Maxwell's equations

$$\nabla \cdot E = 0 \tag{18a}$$

$$\nabla \times E = -\frac{\partial B}{\partial t} \tag{18b}$$

$$\nabla \cdot B = 0 \tag{18c}$$

$$\nabla \times B = \mu_0 \epsilon_0 \frac{\partial E}{\partial t}, \tag{18d}$$

which relate electric fields, E, to magnetic fields, B. The constant ϵ_0 is the electric permittivity and the constant μ_0 is the magnetic permeability.

The derivation starts with Faraday's Law. Take the curl on both sides of (18b):

$$\nabla \times (\nabla \times E) = \nabla \times \left(-\frac{\partial B}{\partial t} \right),$$

and apply the identity $\nabla \times (\nabla \times E) = \nabla(\nabla \cdot E) - \nabla^2 E$

$$\nabla(\nabla \cdot E) - \nabla^2 E = -\frac{\partial \nabla \times B}{\partial t} = -\frac{\partial}{\partial t}\left(\mu_0 \epsilon_0 \frac{\partial E}{\partial t} \right) = -\mu_0 \epsilon_0 \frac{\partial^2 E}{\partial t^2}.$$

Finally, use (18a) to write

$$-\nabla^2 E = -\mu_0 \epsilon_0 \frac{\partial^2 E}{\partial t^2}. \tag{19}$$

Equation (19) shares the general form of a wave equation, $\nabla^2 \psi = 1/v^2 \psi_{tt}$, with speed v traveling along the axis of propagation. Since our simulation deals with lasers, which are light waves, $v = c$. When speed coefficients on (19) are equated with those of the general wave equation, $c = \dfrac{1}{\sqrt{\mu_0 \epsilon_0}} = 2.997 \times 10^8$. Plugging this into (19):

$$\nabla^2 E = \frac{1}{c^2} \frac{\partial^2 E}{\partial t^2}. \tag{20}$$

Equation (20) ignores polarization effects including the fact that perpendicular components of the wave do not interfere; this is not a problem since the simulation uses a plane-wave. The laser simulation uses diffracting beams which do not spread too fast - see Assumption 2. Pressure equalizes quickly and changes in gas density are linearly related to changes in temperature [47].

A further simplification is to assume that ω, the temporal frequency, is constant. As laser-beams are very directional the field can be written as

$$E = \tilde{E}(x, y, z) e^{i\omega t} \tag{21}$$

where the plane wave is factored out. All of the temporal oscillations are covered in $e^{i\omega t}$. $\tilde{E}(x, y, z)$ varies slowly which controls the diameter and strength of the beam as it propagates.

Twice differentiating (21) with respect to t gives

$$\frac{\partial^2 E}{\partial t^2} = -\omega^2 \tilde{E} e^{i\omega t}.$$

Substituting this is into (20) gives

$$c^2 \nabla^2 \tilde{E} e^{i\omega t} = -\omega^2 \tilde{E} e^{i\omega t}. \tag{22}$$

$e^{i\omega t}$, the time dependency, cancels out and we define

$$\eta^2 k^2 = \frac{\omega^2}{c^2},$$

where k is the spatial wave number and $\eta = \eta_0 + \epsilon^2 \eta_1$ is the refractive index; η_0 is the initial refractive index and η_1 is the changes in refractive index induced by the laser beam's interaction with the medium.

Then η and k are used in(22) to get the reduced wave equation:

$$\eta^2 k^2 \tilde{E} + \nabla^2 \tilde{E} = 0. \tag{23}$$

Now the leading term of η is used in the expansion of (23):

$$\tilde{E} = \mathrm{A}(\epsilon x, \epsilon y, \epsilon^2 z) e^{ik\eta_0 z}, \tag{24}$$

where $e^{ik\eta_0 z}$ is the plane wave, slowly varying as indicated by its dependence on $\epsilon x, \epsilon y$, and $\epsilon^2 z$, and A is the amplitude of the wave. We use (23) in (24) to get the asymptotic

expansion

$$\epsilon\left(-k^2\eta_0^2\mathrm{A}e^{ik\eta_0 z}+k^2\eta_0^2\mathrm{A}e^{ik\eta_0 z}\right)+\epsilon^2\left(2ik\eta_0\frac{\partial \mathrm{A}}{\partial z}+\nabla^2\mathrm{A}+2\eta_0\eta_1k^2\mathrm{A}\right)e^{ik\eta_0 z}=0.$$

Clearly the $O(\epsilon)$ term is zero. That means that $O(\epsilon^2)$ is the leading order and the paraxial equation is given by:

$$\left(2ik\eta_0\frac{\partial}{\partial z}-\nabla^2+2\eta_0\eta_1k^2\right)\mathrm{A}=0 \tag{25}$$

Beam intensity from the Paraxial equation is used in the optical fluids solver. Fluid temperature changes due to the laser affect the index of refraction in the laser simulation. Refractive index is discussed in the following section.

Index of Refraction.

Temperature is not directly input into equation (25), but refractive index η is. Some approaches to defining refractive index are discussed in this section.

Ciddor, in [53], provides a model for predicting refractivity of air based on inputs of temperature, pressure, humidity, vapor pressure, and wavelength.

Pries, in [33], provides general rules of refractive, absorption and scattering index values based on time of day and geographic location without providing specific values. The rules are useful for determining reasonable ranges.

Sprangle and Peñano provide a set of values for absorption and scattering index values for various environments in [54]. This is our primary source for choosing values of β_a and β_s.

The Gladstone-Dale relationship gives

$$\eta_1=(1-\eta_0)\frac{\rho_1}{\rho_0},$$

which relates the change in refractive index to the rate of density change [55]. But the Boussinesq assumption means that density changes can be ignored in favor of temperature. For optical frequencies the refractive index depends almost entirely on temperature rather than density [56, 42]. Mathematically, this means

$$\eta_1 = (1 - \eta_0)\frac{T_1}{T_0}, \tag{26}$$

showing the relationship between the change in temperature to the change in refractive index [40] used in the coupled laser-fluid simulation. (26) is used to update η_1 in (6) from temperature changes found using (13).

The exclusive reliance on temperature in (26) is useful for the current study, but it may be useful to include medium characteristics and wavelength of energy in future work. As a possible choice Andrews, in [1], relates pressure and temperature to refractive index with

$$\eta(\mathbf{x}) = 1 + 77.6 \times 10^{-6} \left(1 + 7.52 \times 10^{-3}\lambda^{-2}\right) \frac{P(\mathbf{x})}{T(\mathbf{x})},$$

where λ is the optical wavelength in μm and $P(\mathbf{x})$ is the pressure at a point in space and $T(\mathbf{x})$ is a temperature at a point in space.

The refractive index model employed can can be left open to discussion since it is not much work to change the refractive index function in the simulation. But (26) is used in the simulations for this study, and the particulars of the simulation are provided in the next section.

Simulating the Paraxial Equation.

For all studies in this dissertation the Paraxial Equation, (25), is simulated using spectral methods. This section provides a discussion of the methodology.

Let $\widehat{\mathrm{A}}$ represent the Fourier transform of A and $\check{\mathrm{A}}$ the inverse Fourier transform of A, then the solution of the Paraxial Equation is

$$-2i\widehat{\mathrm{A}_z} + (-k_1^2\widehat{\mathrm{A}} - k_2^2\widehat{\mathrm{A}}) + \widehat{\eta\mathrm{A}} = 0 \tag{27}$$

an infinite system of ordinary differential equations in $\widehat{\mathrm{A}}$. To choose an ordinary differential equation (ODE) solver write

$$\frac{d\widehat{\mathrm{A}}}{dz} = F(\widehat{\mathrm{A}})$$

where

$$F(\widehat{\mathrm{A}}) = -ik_1^2\widehat{\mathrm{A}} - ik_2^2\widehat{\mathrm{A}} + \widehat{\eta\mathrm{A}}.$$

The appropriate ODE solver is dictated by the eigenvalues, $\lambda \in \Lambda(J)$, of J where

$$J = \frac{\partial F}{\partial \widehat{\mathrm{A}}} = \frac{ik_1^2 + ik_2^2}{2} + \frac{\partial}{\partial \widehat{\mathrm{A}}} i\widehat{\eta\mathrm{A}}.$$

For a constant medium $\dfrac{ik_1^2 + ik_2^2}{2}$ form a diagonal matrix, so finding the eigenvalues is easy:

$$\lambda_j = \frac{ik_1^2 + ik_2^2}{2} + i\eta_0$$

for all j in the system. To find the eigenvalues of F, think of

$$G_1 = \frac{\partial}{\partial \widehat{\mathrm{A}}} i\widehat{\eta_1\mathrm{A}}$$

as a perturbation of the eigenvalues, and so long as the perturbation is small the Gerschgoren Disc Theorem can be invoked. If G_1 is small then the perturbed eigenvalues are small. Therefore $\lambda_j \in i\mathbb{R} + O(G_1)$ for all j. To ensure a stable numerical solution to (27) select a step size to keep λ_j on the imaginary axis. In order to incorporate

a large portion of the imaginary axis, and be explicit, Runge-Kutta (RK) family of numerical solvers are elected to advance the solution through time; RK-6 gives a wide range of spatial step sizes leading to stability in the numerical simulation. Figure 3 illustrates the stability region of for RK-6.

Assuming all quantities vary slower in the propagation direction, z, than in the x, y directions justifies neglecting fluid velocities in the z-direction. An asymptotic argument demonstrates this: Recall that (13) employs the forcing $\mathrm{A}(\epsilon x, \epsilon y, \epsilon^2 z)$ from (24). For initially quiescent medium, where $\mathbf{u}_0 = 0$, the scaling for A must be related to the scaling for $\mathbf{u}(X, Y, Z)$. Specifically,

$$X = \frac{1}{\epsilon}x, Y = \frac{1}{\epsilon}y, Z = \frac{1}{\epsilon^2}z.$$

Defining

$$\mathbf{u}(X, Y, Z) = \begin{bmatrix} u(X, Y, Z) \\ v(X, Y, Z) \\ w(X, Y, Z) \end{bmatrix}$$

then, by the chain rule, gives

$$\nabla \cdot \mathbf{u}(X, Y, Z) = \frac{1}{\epsilon}u_x + \frac{1}{\epsilon}v_y + \frac{1}{\epsilon^2}w_z = 0$$

Clearly as $\epsilon \to 0$ $1/\epsilon^2 \to \infty$ much faster than $1/\epsilon$. Thus, via the conservation equation, it is concluded

$$\frac{1}{\epsilon^2}w_z = 0.$$

At next order $\nabla \cdot \mathbf{u} = 0$, thus $1/\epsilon\,(u_x + v_y) = 0$, leaving $w_z = 0$ again. So w must be constant. The boundary conditions further constrain $w = 0$. Therefore the fluid velocity in the z-direction can be neglected.

To simulate the refractive index evolving in the paraxial equation the simulation

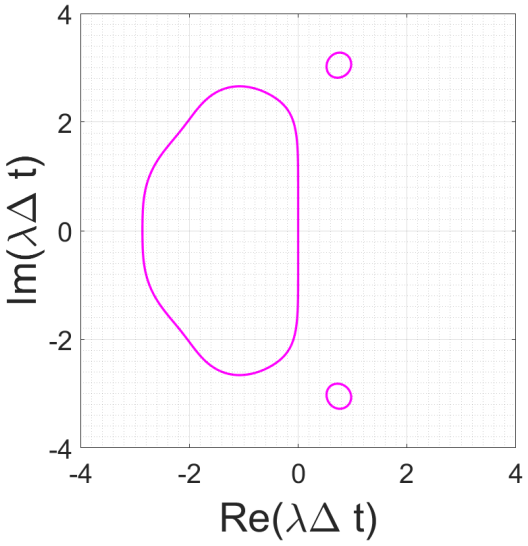

Figure 3. Plot of the stability region for Runge-Kutta sixth order numerical scheme (RK-6). Inside the closed shapes the ODE is numerically stable. RK-6 includes a large portion of the imaginary axis, therefore a large number of step sizes that ensure numerical stability are available.

interpolates between temperature fields, from (13), in transverse 2-D time slices at the start and end of the volume through which the laser is propagating. Convergence of the interpolation method is covered in the in the next section. The complete numerical scheme is covered in detail in Chapter III.

Convergence Analysis.

Linear interpolation is used between two-dimensional instances of fluid temperature obtained from the Boussinesq approximation of the optical fluid. This gives the laser intensity an $O(dz^2)$ convergence as the characteristic space step along the propagation axis, dz, goes to zero over the propagation distance, L. Figure 4 shows the convergence of Cauchy error between laser simulations with decreasing dz over the whole propagation domain.

The optical fluid solver and the simulation of beam propagation need to be coupled together. Tying the two models together relies on passing two-dimensional tempera-

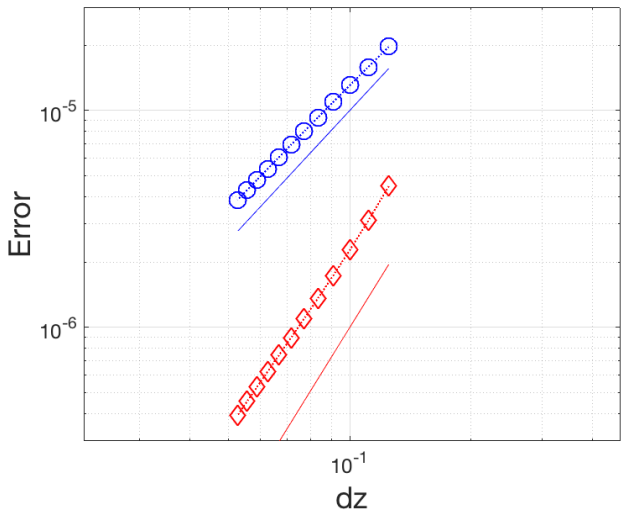

Figure 4. Plot of Cauchy error of Paraxial Simulation using interpolation; dz is the interpolation cell width along the axis of beam propagation, the z axis. The y-axis is the Cauchy error computed by taking the Euclidean norm of the difference of two consecutive estimates. Circles denote error from linear interpolation between screens; it is parallel to the $m = 2$ reference line showing that interpolation error converges on $O(dz^2)$. Diamonds denote error from quadratic interpolation between screens; it is parallel to the $m = 3$ reference line showing that the interpolation error converges on $O(dz^3)$.

ture fields from the numerical fluid solver to the beam propagation simulation interpolates between temperature fields. The details of the coupled model are provided in the next chapter.

III. Coupling Laser-Fluid Model

This chapter describes the predictor-corrector scheme employed to couple the optical fluid solver to the paraxial laser propagation simulation, illustrated in Figure 5.

Equations (25) and (13) are evolved together using a predictor corrector scheme coupled to the spectral simulation of the paraxial laser propagation equation. A is initialized with a Gaussian beam

$$A(x, y, 0) = e^{-x^2-y^2}.$$

Temperature is initialized as $T(x, y, z; 0) = 0$, and velocity is initialized as $\mathbf{u}(x, y, z; 0) = 0$. Laser beam intensity is passed to (13), where fluid temperature is evolved on transverse two dimensional slices for a half time-step, $\Delta t/2$, to get a predicted temperature. The predicted temperature is then used in (25) to get a predicted intensity, which is then used in (13) to get temperature as evolved over the full time-step, Δt. This full time temperature is finally used in (25) to get a corrected beam intensity over Δz. We advance time and space and begin again. This process is illustrated in Figure 5.

The initial conditions for the coupled solver are covered in the next section, and the convergence of the entire simulation in Section 3.2.

3.1 Initial Conditions

We initialize the laser beam as a Gaussian beam with constant phase.

For the boundary conditions study in Chapter IV the fluid initial conditions are $\mathbf{u}(\mathbf{x}, 0) = 0$ and $T(\mathbf{x}, 0) = 0$.

The following section provides a convergence study for finite box boundary conditions. Chapter IV is devoted to a boundary conditions study.

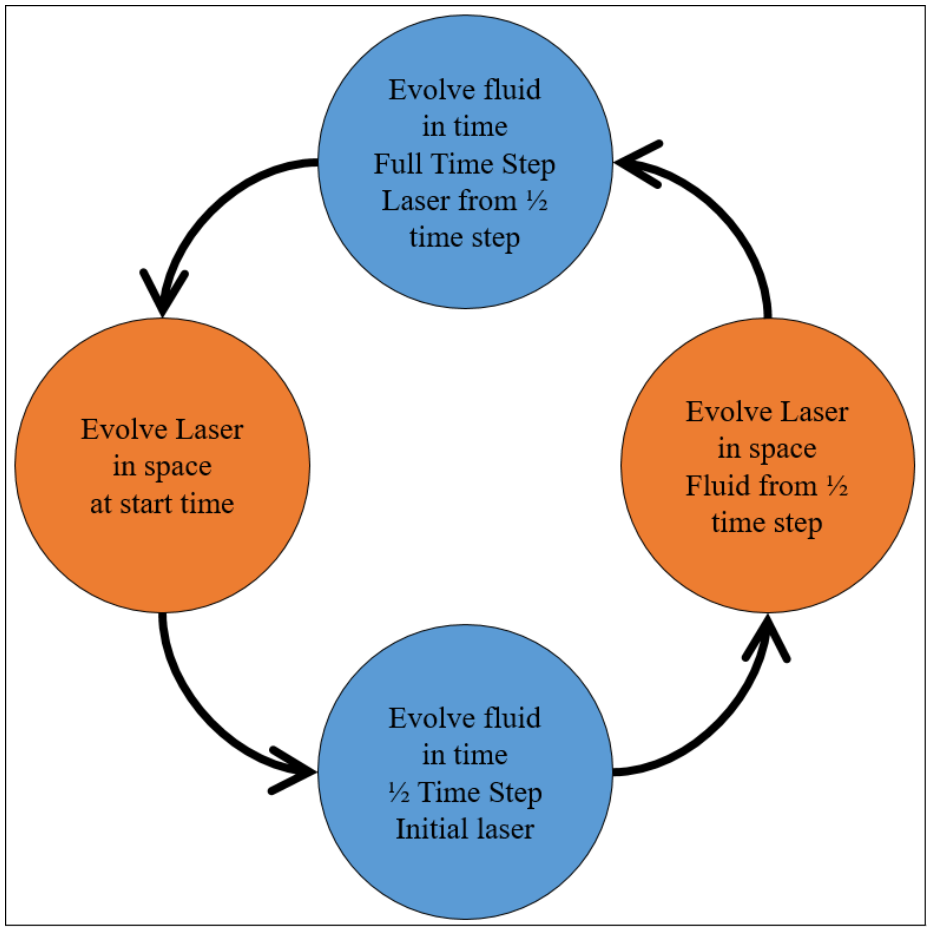

Figure 5. Flowchart showing the relationship between the numerical solver for the Boussinesq equations and the Paraxial equation. The whole cycle begins with the introduction of A_0 to the Boussinesq solver. The system iterates using A_0 each time since we require the source intensity for every time step.

3.2 Coupled Solver Convergence

Figure 6 shows Cauchy error of temperature on the left and intensity on the right. Cauchy error is defined as $\|T_{\delta\tau_{i-1}} - T_{\delta\tau_i}\|_\infty$ for $i = 2, 3, \ldots, 5$ where $T_{\delta\tau_i}$ is the temperature approximated with the ith splitting time step, $\Delta\tau$, and $T_{\delta\tau_{i-1}}$ is temperature approximated using the previous splitting time step. Similarly the Cauchy error for HEL intensity is $\|T_{\delta\tau_{i-1}} - T_{\delta\tau_i}\|_\infty$ for $i = 2, 3, \ldots, 5$. Cauchy error of the approximation converges to zero at the same rate as the true error of the simulation using decreasing splitting time steps.

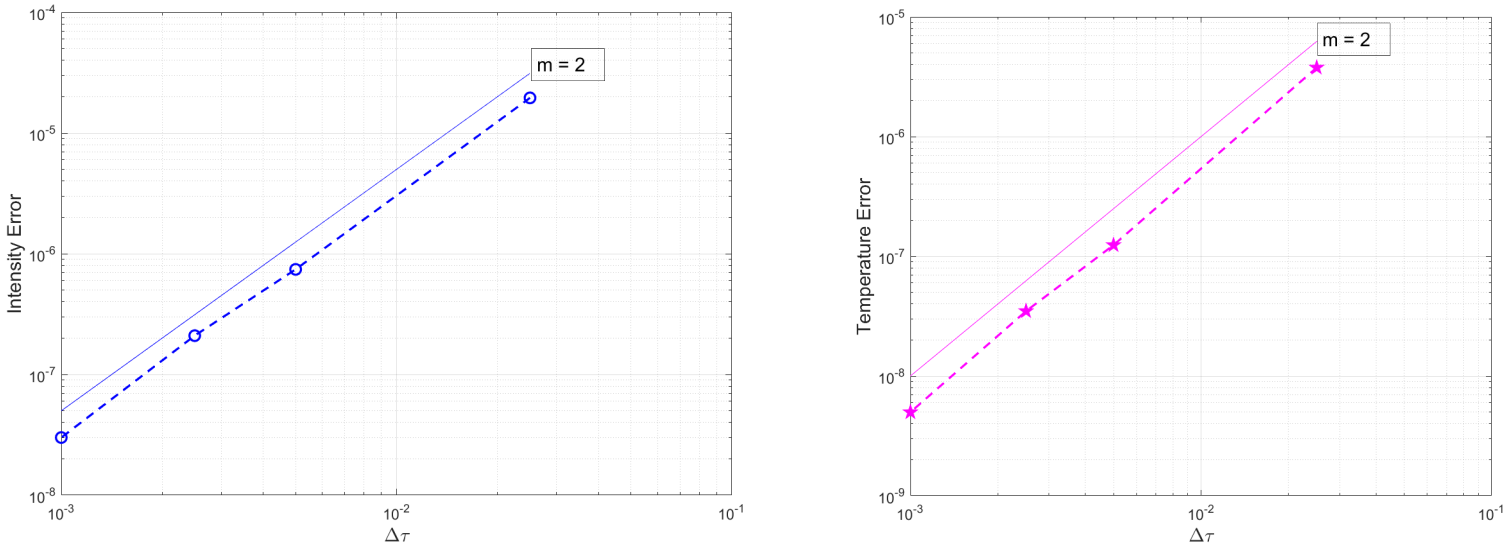

Figure 6. Left: Cauchy error convergence for intensity at $L_z = 100$ and over $T_f = 0.3$ for decreasing coupled model splitting time step, $\Delta\tau$. Right: Cauchy error convergence for temperature at $L_z = 100$ and over $T_f = 0.3$ for decreasing coupled model splitting time step, $\Delta\tau$.

Boundary conditions are discussed in greater detail in the next chapter, but convergence of the coupled laser-fluid model can be shown with finite box boundary conditions. Where

$$v = 0; \qquad \frac{\partial u}{\partial y} = 0 \text{ on top and bottom,}$$

$$u = 0; \qquad \frac{\partial v}{\partial x} = 0 \text{ on the sides,}$$

for $\mathbf{u} = [u, v, 0]$, and the boundaries of the fluid temperature are zero flux, that is $T_x = T_y = 0$ on the boundary.

The coupled laser-fluid solver is run over a propagation distance of $L_z = 100$ and over time $T_f = 0.3$ with splitting time steps, $\Delta\tau$. Cauchy error of the temperature and the intensity is measured for each $\Delta\tau$. The results are shown in Figure 6 for decreasing outer time step $\Delta\tau$ - the time over which (13) is evolved for each iteration.

Figure 6 shows that the predictor corrector method has $O(\Delta\tau^2)$ convergence. The

effects of boundary conditions on the accuracy of the coupled laser-fluid model are discussed in the following chapter.

IV. Boundary Conditions

4.1 Introduction

Equation (13) is used to simulate fluid dynamics in free space - a physically unbounded domain. In order to simulate such a domain it is typical to artificially truncate the domain to finite dimensions and apply open boundary conditions (OBC) on the artificial boundary. OBC's are a difficult problem [57, 58, 59]. Traction free boundary conditions and radiation boundary conditions are two commonly applied conditions to simulate OBC's [60, 61, 62, 63, 57, 64, 65, 66, 67, 58, 68, 69, 70, 71]. At high Reynolds numbers (Re = 300 to 400) back-flow instabilities develop and cause numerical simulations to blow up under these boundary conditions [72]. Taylor, Rance and Medwell present a methodology for implementing traction boundary conditions that overcome back-flow instabilities, but the method fails when disturbances develop upstream from the outflow boundary [73]. Prevalent methodology has been to asymptotically increase a large finite boundary box to give the vortices time and space to dissipate before reaching the box's edge. This becomes problematic as the Reynolds number increases so does the required size of the box until computation time balloons beyond control [59]. We can make computational costs more tractable by imposing periodic boundary conditions and applying spectral methods to numerically solve NSE [49]. These are not physically representative, though.

OBC's have been developed in order to allow for smaller domains without worrying about back-flow instabilities. These typically fall under two categories: one-sided differencing and Newtonian damping, or sponge layer, at the boundary. One-sided differencing methods were popular in the 1960's, but it has been shown that they develop reflections and instabilities when large disturbances were analyzed. Absorbing layers has been very popular and used in analyzing small scale flows, but produce

reflections due to variations of viscosity on the boundary. In the past Newtonian damping has been used to force the solution to a known boundary condition, but waves traveling tangential to the boundary tend to be distorted by spatial variations or damping [67]. Current developments to address issues of reflection at the boundary require either the boundary conditions to be known, or for the solver to approximate their value [63, 60, 74, 68, 62, 75, 76]. Perfectly matched layers have been used to successfully reduce reflection at the artificial outflow boundary [69, 77, 78, 70, 72, 59]. But absorbing boundaries and perfectly matched layers methods fail to address disturbance that develop at the boundary and reenter the domain.

In [16] Fornberg outlines a method for addressing open boundaries that is accurate for high Reynolds numbers (up to 600). Implementation of Fornberg's method is described in Section 4.2; it is further compared to periodic boundary conditions and finite box boundary conditions. Nataf, in [79], compares a similar method to Fornberg's, but did not provide rigorous analysis of the method spelled out in [16, 80].

The remainder of the section is organized as follows. Formulation of the problem with an explanation of the laser-fluid numerical method is laid out in Section 4.2. Then in Section 4.3 numerical simulation results are provided. Section 4.4 presents conclusions of the boundary condition study.

4.2 Formulation

Non-dimensionalized Navier-Stokes equations, (13), are used to dynamically model fluid-beam interaction with a forcing expression for temperature driven by HEL beam intensity, A, given by the paraxial or, Schrödinger's equation (25). For the boundary conditions study (13) is changed to stream-function vorticity form.

To transform (13) into stream-function vorticity form the curl of (13a) and (13c)

is taken

$$\nabla \times [\mathbf{u}_t + (\mathbf{u} \cdot \nabla)\mathbf{u}] = \nabla \times \left(\nabla P + \frac{1}{Re} \nabla^2 \mathbf{u} + RiT\mathbf{e}_2 \right) \tag{28}$$

$$\nabla \times (\nabla \cdot \mathbf{u}) = 0. \tag{29}$$

(13b) can be handled with a substitution so it will be addressed at the end of the derivation. Vorticity, ω, is defined as $\omega = \nabla \times \mathbf{u}$ where $\mathbf{u} = [u, v, 0]'$, so that

$$\nabla \times \mathbf{u} = \begin{bmatrix} 0 \\ 0 \\ v_x - u_y \end{bmatrix}.$$

This suggests that we need only consider the third component of vorticity, $\omega = v_x - u_y$, as a scalar. The following simplifications are made for the terms of (28):

$$\nabla \times \mathbf{u}_t = \omega_t,$$

$$\nabla \times (\nabla P) = 0,$$

$$\frac{1}{Re} \nabla \times \nabla^2 \mathbf{u} = \frac{1}{Re} \nabla^2 (\nabla \times \mathbf{u}) = \frac{1}{Re} \nabla^2 \omega,$$

$$\nabla \times RiT\mathbf{e}_2 = -RiT_x \mathbf{e}_2.$$

A more involved series of substitutions and simplifications are required for the non-linear term of (28), $\nabla \times [(\mathbf{u} \cdot \nabla)\mathbf{u}]$; specifically the identity

$$(\mathbf{u} \cdot \nabla)\mathbf{u} = (\nabla \times \mathbf{u}) \times \mathbf{u} + \nabla \left(\frac{1}{2} \mathbf{u} \cdot \mathbf{u} \right)$$

is required, into which vorticity is substituted to give

$$(\mathbf{u} \cdot \nabla)\mathbf{u} = \omega \times \mathbf{u} + \nabla \left(\frac{1}{2} \mathbf{u} \cdot \mathbf{u} \right); \tag{30}$$

(30) is substituted into $\nabla \times [(\mathbf{u} \cdot \nabla)\mathbf{u}]$ to yeild

$$\nabla \times [(\mathbf{u} \cdot \nabla)\mathbf{u}] = \nabla \times \left[\omega \times \mathbf{u} + \nabla\left(\frac{1}{2}\mathbf{u} \cdot \mathbf{u}\right)\right]$$

$$= \nabla \times (\omega \times \mathbf{u}) + \nabla \times \left(\nabla\left[\frac{1}{2}\mathbf{u} \cdot \mathbf{u}\right]\right) = \nabla \times (\omega \times \mathbf{u})$$

by the product rule. Now applying the divergence free condition (13c) gives

$$\nabla \times [(\mathbf{u} \cdot \nabla)\mathbf{u}] = \nabla \times (\omega \times \mathbf{u}) = (\mathbf{u} \cdot \nabla)\omega.$$

Substituting all of these simplifications into (28) gives

$$\omega_t + (\mathbf{u} \cdot \nabla)\omega = \frac{1}{Re}\nabla^2\omega - RiT_x\mathbf{e}_2. \tag{31}$$

The stream function, ψ, is defined so that $u = \psi_y$ and $v = -\psi_x$. That is ψ is defined with a path integral on a path, p, over which ψ is path independent

$$\psi = \int_p udy - vdx. \tag{32}$$

This means that $u_x = -v_y$ is written $u_x + v_y = \nabla \cdot \mathbf{u} = 0$, making it unnecessary to carry (29) since the definition of ψ in (32) ensures zero divergence.

Substituting (32) into (31) and (13b) completes the derivation of the stream-function vorticity form of (13)

$$\omega_t + \left(\psi_x\frac{\partial}{\partial y} - \psi_y\frac{\partial}{\partial x}\right)\omega = \frac{1}{Re}\nabla^2\omega - RiT_x\mathbf{e}_2 \tag{33a}$$

$$T_t + \left(\psi_x\frac{\partial}{\partial y} - \psi_y\frac{\partial}{\partial x}\right)T = \frac{1}{Pe}\nabla^2 T + St|A|^2. \tag{33b}$$

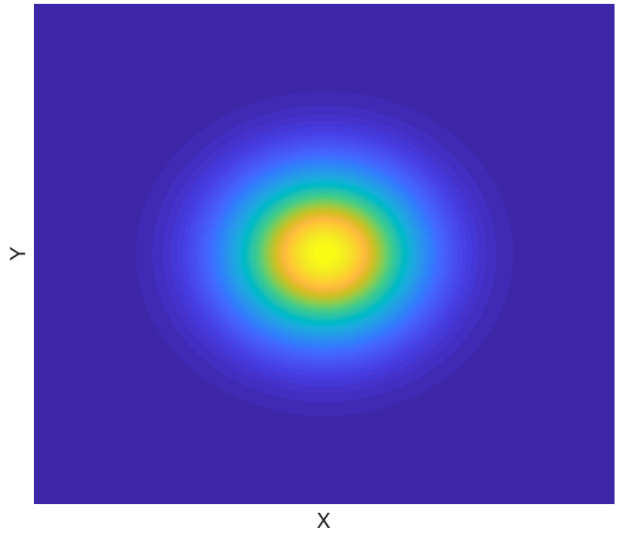

Figure 7. Initial beam profile for the laser-fluid coupled solver.

Note that (25) uses $\eta_1 = (1-\eta_0)T/T_0$, the absorptivity coefficient, which depends on the fluid temperature output from (33).

Equations (33) and (25) are evolved together using a predictor-corrector scheme coupled to the spectral simulation of (25). A is initialized with a Gaussian beam

$$A(x, y, 0) = e^{-x^2-x^2}.$$

Temperature is initialized as $T(x, y, z; 0) = 0$, and velocity is initialized as $\mathbf{u}(x, y, z; 0) = 0$; therefore $\omega = \psi = 0$, as in Figure 7.

Intensity is passed to (25), where it is evolved on two dimensional transverse slices for a half time-step, $\Delta t/2$, to get a predicted temperature. The predicted temperature is then evolved for a full space step, Δt, in (25) to get a predicted intensity, which is then used in (33) to get temperature as evolved over a full time-step, Δt. This temperature at Δt is finally used in (25) to get a corrected beam intensity over the volume of propagation distance Δz. Time and space a steps are advanced and the

cycle begins again. This process is illustrated in Figure 5.

Three approaches to modeling free space boundary conditions for laser beam-fluid interaction are discussed:

1. Periodic boundary conditions

$$\mathbf{u}(\mathbf{x}+L,t)=\mathbf{u}(\mathbf{x},t)$$

$$T(\mathbf{x}+L,t)=T(\mathbf{x},t)$$

$$P(\mathbf{x}+L,t)=P(\mathbf{x},t)$$

2. Slip boundary conditions in a finite box

$$v=0; \qquad \frac{\partial u}{\partial y}=0 \text{ on top and bottom}$$

$$u=0; \qquad \frac{\partial v}{\partial x}=0 \text{ on the sides}$$

$$\frac{\partial T}{\partial x}=0; \qquad \frac{\partial T}{\partial y}=0$$

$$P=v\frac{\partial u}{\partial y}=0 \text{ on top and bottom}$$

$$P=u\frac{\partial v}{\partial x}=0 \text{ on the sides}$$

3. Fornberg's open boundary (FOB) conditions taken from [16]

$$\mathscr{L}\Psi_E=\Psi_I$$

$$\frac{\partial T}{\partial x}=0; \qquad \frac{\partial T}{\partial y}=0$$

Periodic boundary conditions use a spectral solver to numerically solve (33) to

reduce the impact on computation time of increase the size of the period on the bounds. Implementation of periodic boundary conditions follow the methodology laid out by Akers and Reeger in [49]. The Fast Fourier transform allows for faster computations, but periodic boundary conditions are not physical. Periodic boundary conditions essentially assume an infinite array of beam intensity spots, or a torus shaped domain. Fluid heated by the beam convects vertically to the top of the period and continues through the bottom of the period creating errors in the fluid simulation.

Slip boundary conditions and free-space boundary conditions are implemented with finite difference methods. Second-order up-winding is applied to approximate the nonlinear terms in (33a) and (33b), using the method from [48]. Linear terms are updated via second-order finite-differencing methods and ψ is updated in (33a) by

$$\nabla^2 \psi = \omega \tag{34}$$

using a Poisson's equation solver similar to pressure correction schemes. The finite box boundary conditions, although physical, may not be the boundary conditions needed for this problem.

The focus of this study is on FOB conditions. In this work FOB conditions are implemented with a finite difference scheme.

The system (33) is stated in stream-function vorticity form so that localization of vorticity can be exploited. In the free-space laser-fluid problem, $\psi \to 0$ more slowly than $\omega \to 0$ as $\|\mathbf{x}\| \to \infty$. The slow decay rate of *psi* is based on the fundamental solution to (36), which is $\Psi(\|\mathbf{x}\|_2) = \ln(\|\mathbf{x}\|_2)$ in two-dimensions. The faster decay rate, i.e. exponential decay, of ω is based on observations [80].

A finite sub-domain, Ω_F, is defined in the infinite domain. Taking advantage of the fact that ω decays quickly Ω_F is chosen so that $\Delta\psi$ is approximately zero on the

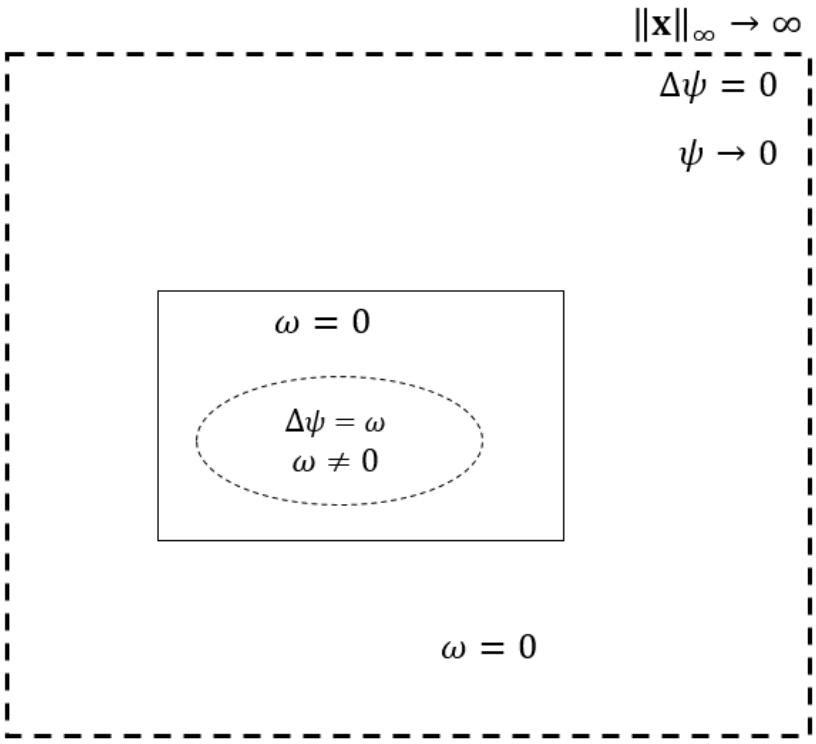

Figure 8. Cartoon of FOB conditions showing $\omega \to 0$ quickly and $\psi \to 0$ slowly as $\mathbf{x} \to \infty$. Note the finite domain where $\omega \neq 0$ is localized, shown by the dotted line. The solid line denotes the finite sub-domain where open boundary conditions-informed fluid behavior is approximated.

boundary of Ω_F. This is illustrated in Figure 8 by the solid rectangle.

N points, X_E, are chosen on the exterior of Ω_F so that $\nabla^2\psi(X_E)$ is approximately zero, where $\psi(X_E)$ is the stream-function evaluated at the points of X_E. N more points are chosen, X_I, from the interior of Ω_F. Selecting N points for X_I requires a choice at the four corners of X_I in order to get the points of X_E and X_I to closely line up. The points of vectors X_E and X_I are illustrated in Figure 9.

It is essential for X_E and X_I to have the same number of points so that a linear relation can be defined as

$$\mathscr{L}\psi(X_E) = \psi(X_I), \tag{35}$$

where $\mathscr{L}$ is the linear relation and $\psi(X_I)$ is the stream-function evaluated at the points of X_I.

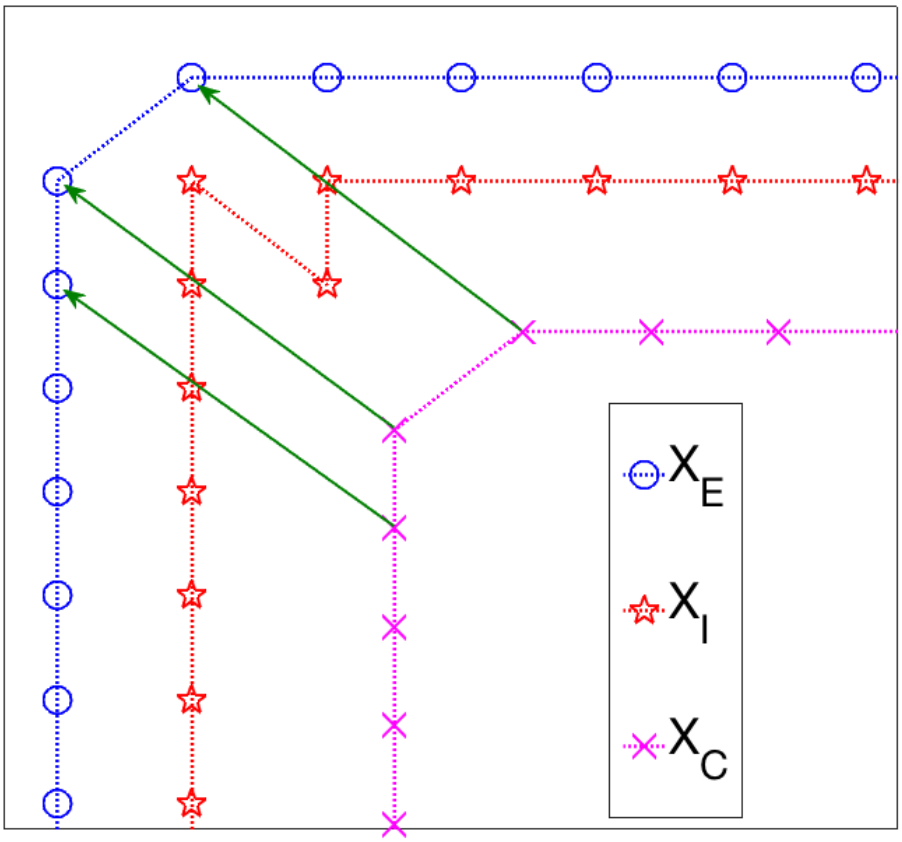

Figure 9. Illustration of grid points selected about the finite sub-domain at which we make our approximation. ◯ denotes X_E, ★ denotes X_I and + denotes X_C. The set X_C is defined by taking a fractional number of Δx sized steps into the finite domain. The dashed arrows illustrate the directional vector $\mathbf{n}_i$ used in defining the basis function.

An additional N points, X_C, are defined as a scaling of X_E so that X_C lies further interior to Ω_F than X_I. This is shown in Figure 9. X_C is defined as

$$X_C = \frac{L - ah}{L} X_E,$$

where L is the length of the virtual bound on a side, h is grid spacing, and a is an ad hoc value describing the number of steps into the virtual bound we take as a ratio of virtual bound size. It works best if $X_I > X_C$ for all values, however the optimal a

has to be recovered by trial and error.

The points of X_C are used to center the basis functions, Ψ. Since $\nabla^2\psi$ is approximately zero at the boundary of Ω_F we select as basis functions the fundamental solution to

$$\nabla^2\Psi = \delta(\|\mathbf{x} - X_C\|_2), \tag{36}$$

where δ is the Dirac delta function, can be described with its fundamental solution for two dimensions $\Psi(\|\mathbf{x}\|_2) = \ln(\|\mathbf{x}\|_2)$. Unfortunately the fundamental solution is not localized.

In order to get a greater decay rate for the basis functions the directional derivative of Ψ is used as the basis function. Since $\nabla^2\Psi = 0 \; \forall \; \mathbf{x} \neq X_C$ implies that $\nabla^2\dfrac{\partial}{\partial\mathbf{n}}\Psi = 0$ $\forall \; \mathbf{x} \neq X_C$, using a basis defined by $\dfrac{\partial}{\partial\mathbf{n}}\Psi$ satisfies $\nabla^2\psi \approx 0$ on the boundary of Ω_F.

Basis functions are defined as

$$\frac{\partial\Psi_j}{\partial\mathbf{n}_j}(\mathbf{x}_i) = \frac{\partial\psi(\mathbf{x}_i - X_C)}{\partial\mathbf{n}_j},$$

where Ψ is the fundamental solution to (36). Directional derivatives use the direction vector

$$\mathbf{n}_j = \frac{\mathbf{x}_{E_j} - \mathbf{x}_{C_j}}{\|\mathbf{x}_{E_j} - \mathbf{x}_{C_j}\|_2}.$$

Basis functions are explicitly computed as

$$\frac{\partial\Psi_j}{\partial\mathbf{n}_j}(\mathbf{x}_i) = \mathbf{n}_j \cdot \begin{bmatrix} \frac{x - x_{C_j}}{(x-x_{C_j})^2 + (y-y_{C_j})^2} \\ \frac{y - y_{C_j}}{(x-x_{C_j})^2 + (y-y_{C_j})^2} \end{bmatrix},$$

where $(x_{C_j}, y_{C_j}) \in X_C$ for $j = 1, \ldots, N$. Figure 10 shows that $\dfrac{\partial\Psi_j}{\partial\mathbf{n}_j}$ decays quickly to zero for $\mathbf{x} \neq X_C$.

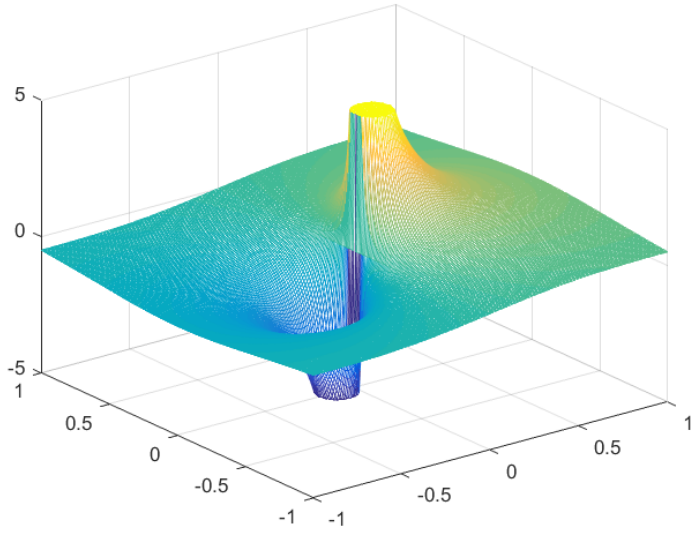

Figure 10. Mesh plot of the basis function $\frac{\partial \Psi_j}{\partial \mathbf{n}_j}(\mathbf{x}_i)$. Note the rapid decay of the function for x further from X_C.

Applying the set of basis functions to (35) gives

$$\mathscr{L}\left[\frac{\partial \Psi_j}{\partial \mathbf{n}_j}(X_E)\right] = \left[\frac{\partial \Psi_j}{\partial \mathbf{n}_j}(X_I)\right].$$

Defining

$$\Psi_I = \left[\frac{\partial \Psi_1}{\partial \mathbf{n}_1}(x_{I_i}), \frac{\partial \Psi_2}{\partial \mathbf{n}_2}(x_{I_i}), \ldots \frac{\partial \Psi_{N-2}}{\partial \mathbf{n}_1}(x_{I_{N-2}})\right]; \qquad i = 1, 2, \ldots, N-2$$

and

$$\Psi_E = \left[\frac{\partial \Psi_1}{\partial \mathbf{n}_1}(x_{E_i}), \frac{\partial \Psi_2}{\partial \mathbf{n}_2}(x_{E_i}), \ldots \frac{\partial \Psi_{N-2}}{\partial \mathbf{n}_1}(x_{E_{N-2}})\right]; \qquad i = 1, 2, \ldots, N-2$$

allows (35) to be rewritten as

$$\mathscr{L}\Psi_E = \Psi_I. \tag{37}$$

Figure 11 shows a plot of the $N \times N$ matrix Ψ_E. The selected basis functions ensure

that Ψ_E is diagonal dominant, therefore Ψ_E is invertible.

The relation $\mathscr{L}$ is found by inverting Ψ_E and multiplying the inverse on both sides to get

$$\mathscr{L} = \Psi_I \Psi_E^{-1}.$$

Figure 12 shows the matrix system used to approximate the solution to $\nabla^2\psi = \omega$. In the numerical scheme ω is numerically updated before ψ is updated so the system in Figure 12 is solved by inverting the matrix on the left of the figure. $\mathscr{L}$ is used in the bottom left corner of the matrix depicted in Figure 12 as an $(N-2)\times(N-2)$ separated system. The boundary solution scheme calls only points on the boundary of the Ω_F collected in the sub-matrix in the bottom left of the matrix in Figure 12. The bottom two sub matrices approximate the solution to $\nabla^2\psi = \omega$ on the boundary of Ω_F.

The sub-matrix in the top left of the matrix refers to the points on the interior of Ω_F in order to solve $\nabla^2\psi = \omega$ on the interior of Ω_F. The scheme uses a second order centered difference scheme defined as

$$\omega_{i,j} = \frac{\psi_{i-1,j} - 2\psi_{i,j} + \psi_{i+1,j}}{\Delta x^2} + \frac{\psi_{i,j-1} - 2\psi_{i,j} + \psi_{i,j+1}}{\Delta y^2}.$$

The scheme references points on the boundary of Ω_F shown in the sub-matrix on the top right of the matrix in Figure 12.

Handling the boundary conditions in this way simulates the fluid convection exiting the finite sub-domain without reflection as well as the fluid wrapping back into the finite sub-domain. Stream-function back-flow is allowed by the FOB conditions, but no back-flow is allowed in vorticity. We show this in Figure 13, a plot of a fluid temperature heated by a constant beam intensity at the laser source for full time. Therefore the size of Ω_F should be selected to ensure for vorticity to decay to zero at

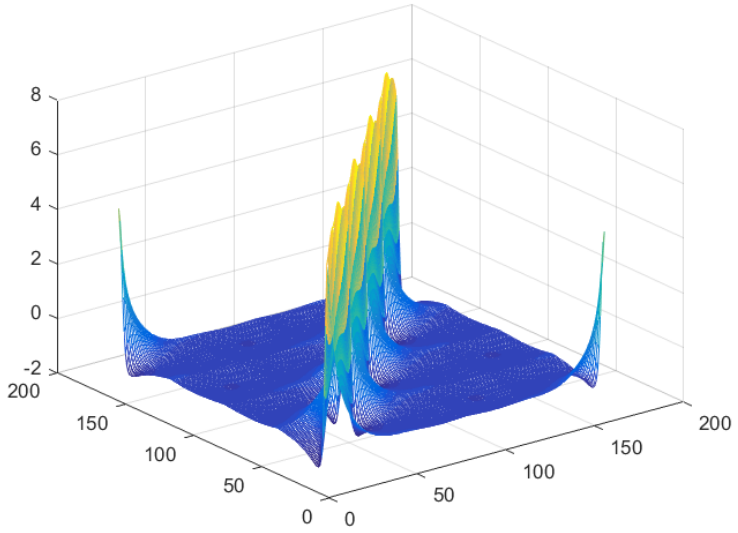

Figure 11. Mesh plot of Ψ_E, the N points of X_E evaluated on the N basis functions $\frac{\partial \Psi_j}{\partial \mathbf{n}_j}(\mathbf{x}_i)$. The selected basis functions makes the matrix Ψ_E diagonal dominant, and therefore invertible. So that the linear relation (37) can be solved.

the boundary.

Asymptotic analysis of the boundary conditions is provided in the next section.

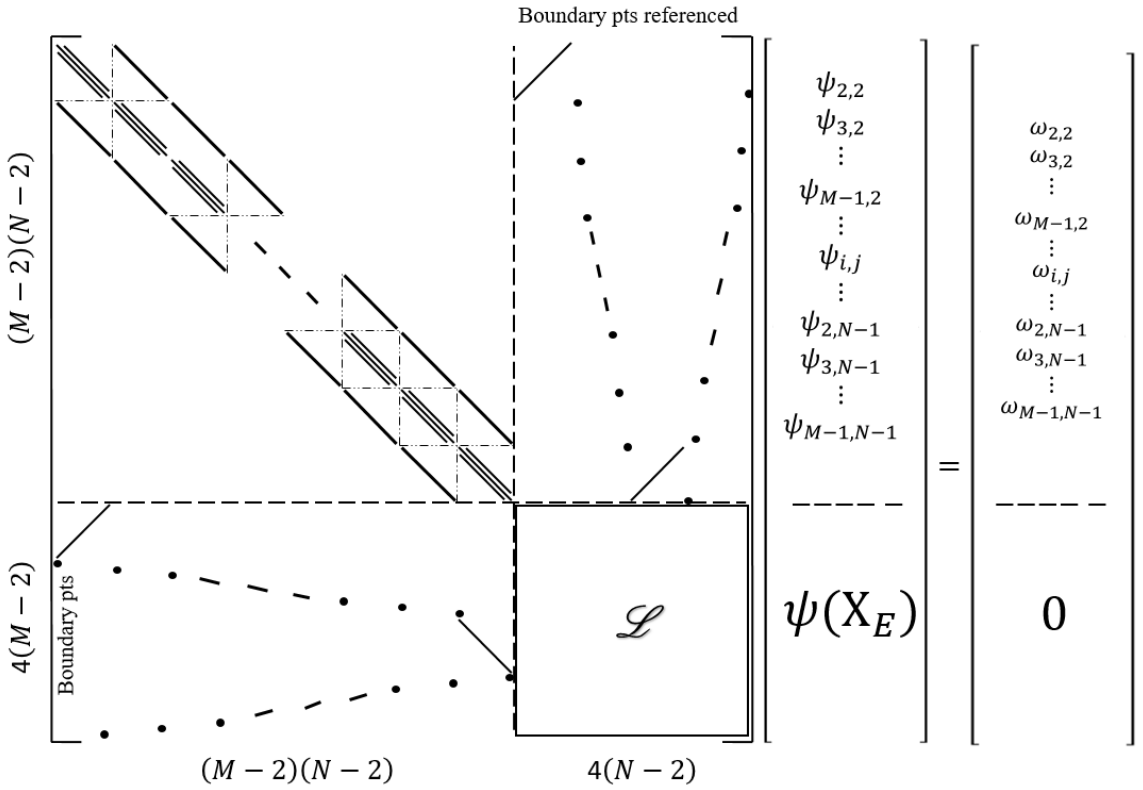

Figure 12. Matrix formulation of numerical method for solving $\nabla^2\psi = \omega$ utilizing $\mathscr{L}$ as an $(N-2)\times(N-2)$ separated system for the boundary of finite sub-domain. The right-hand matrix is inverted to update ψ. $\mathscr{L}$ and the bottom left sub-matrix constitute a sub-system for solving $\nabla^2\psi$ on the boundary of the finite sub-domain. The interior of the sub-domain is solved by the top two sub-matrices.

4.3 Numerical Results

Figure 14 shows the temperature color map for the finite box, periodic and FOB boundary conditions from left to right. The three boundary conditions are shown for increasing boundary sizes to illustrate that the fluid temperature approximation appears to be converging to similar solutions.

Tests for convergence of the boundary conditions assume that fluid temperature and beam intensity will converge as the domain size approaches infinity. Assume a square domain beginning with length $L = 2\pi$ on each side of the domain, and increase the domain size while maintaining a fixed space step of $h = 0.05$. Fourier methods are faster when the number of grid points is a power of 2, so L is incremented by doubling

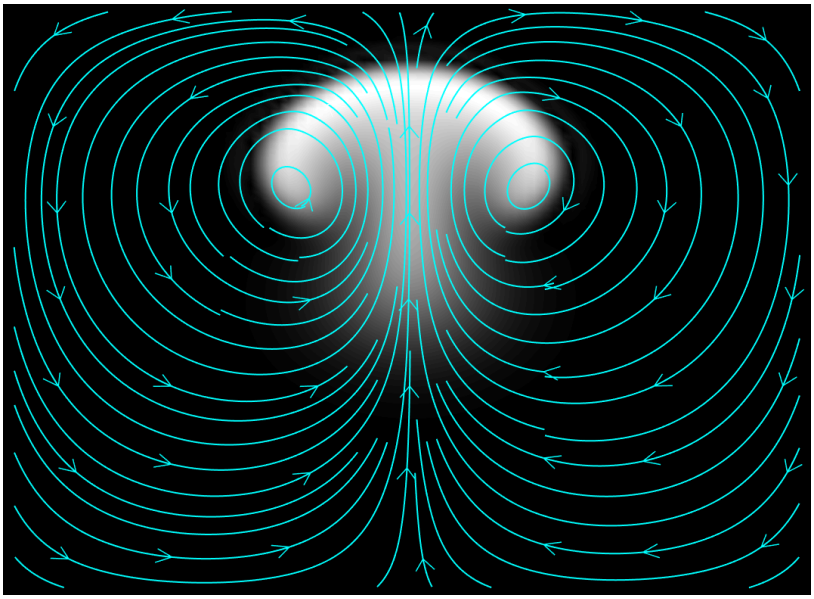

Figure 13. Temperature colormap with fluid stream lines illustrating the fluid velocity leading out of the finite sub-domain – back-flow of the stream function is allowed.

it in each iteration. The free space boundary conditions and finite box boundaries are more flexible in the number of points, but there are limits on storage constraints with respect to how many points can be used for the grid. The Finite difference boundaries are incremented by $20h$ and are limited to $L = 2\pi + 100h$.

Cauchy error was taken between consecutive domain lengths. Temperature results, shown on the right of Figure 15, were taken at laser source. Intensity results, shown on the left of Figure 15, were taken at a distance of 100 units from the laser source.

FOB has the fastest convergence at a rate of $O(L^{-4})$; indeed both of the "correct" boundary conditions perform better than the periodic boundary conditions. Convergence performance must be weighed against the computation costs of the finite difference methods employed for FOB and finite box conditions. Computation times are compared in Figure 16.

Computation times are taken for a fixed domain size while number of grid points are increased on the left of Figure 16. To capture the tradeoff between forcing down error and ballooning computation costs computation time is plotted as a function of

Cauchy error on the right hand side of Figure 16. Simulation time experiments were performed on a Mac Pro with 3.5 Ghz 6-core Intel Xeon E5 Processor.

FOB takes the longest to compute. This is due to the special construction of the solver matrix as well as the necessity of inverting an additional matrix. A fast iterative solver like Matlab's GMRES function was not tested for the finite difference methods since for finite box boundary conditions pre-inverting the matrix and multiplication at each iteration was the same cost as applying GMRES at each iteration; Moreover FOB requires a matrix that does not lend itself well to GMRES.

4.4 Conclusion

Periodic boundary conditions, finite box boundary conditions and FOB were compared. While FOB has the fastest convergence of the boundary conditions evaluated, it can become prohibitively expensive to run for large domains or high resolution.

Periodic boundary conditions allow for Fourier methods which are just too fast too ignore. Error can always be brought down with larger domain sizes and higher resolution with only slightly higher time costs. Thus, periodic boundary conditions are selected in Chapter V as boundary conditions for the numerical fluid solver.

It should be noted, however, that the comparison between the finite box boundary conditions and the periodic boundary conditions is not quite fair. If periodic boundary conditions were evaluated with the finite difference solver, the diamond line in the right hand side of Figure 16 would have the same slope as the line for finite box computation times versus error.

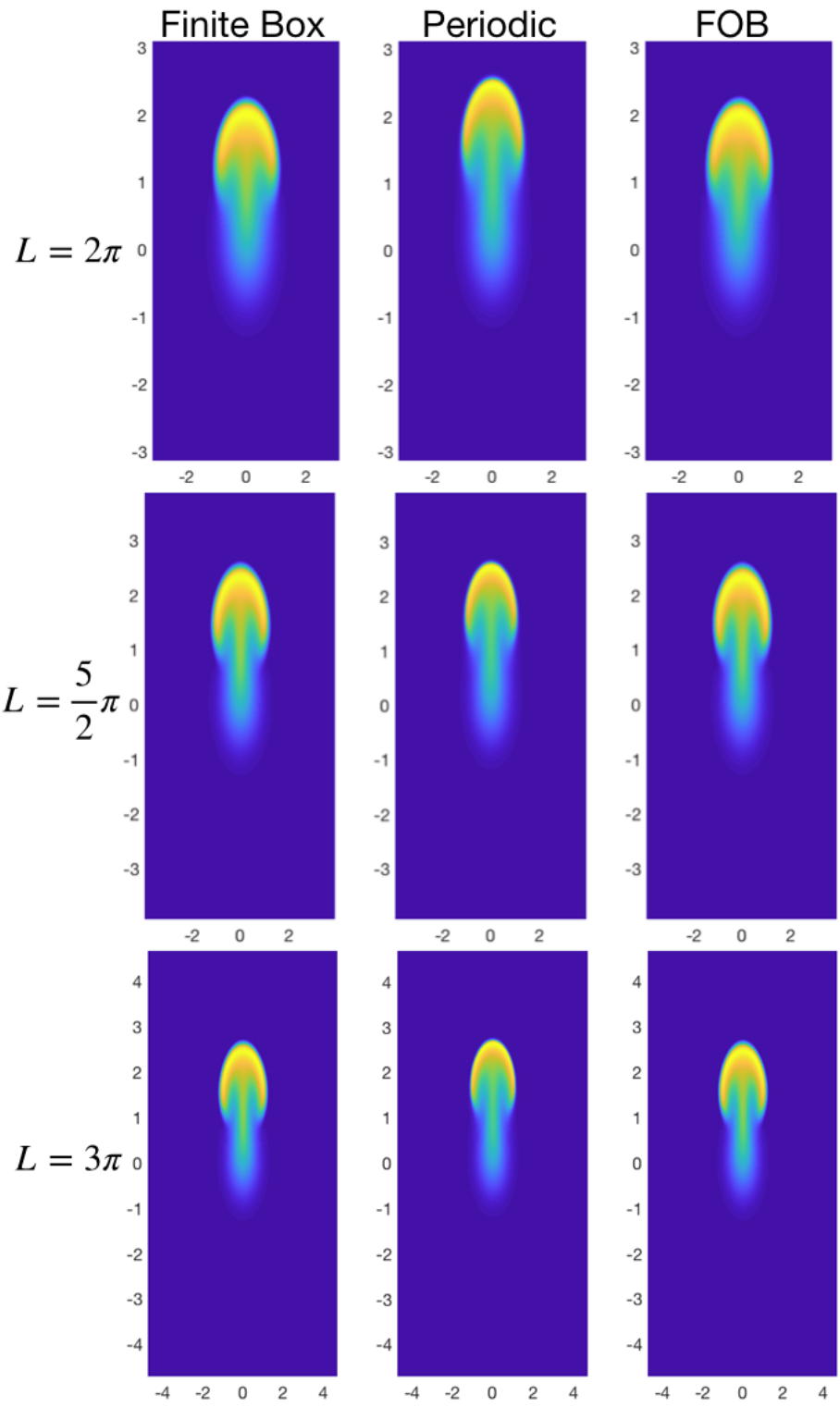

Figure 14. From left to right, the color maps shows fluid temperature approximations using finite box boundary conditions, periodic boundary conditions and FOB boundary conditions. Top row shows the results for L, domain length for a square domain, equal to 2π. Second row shows results for $L = \frac{5}{2}\pi$. Third row shows results for $L = 3\pi$. The numerical approximations using the three boundary conditions appear to converge to similar solutions as L increases.

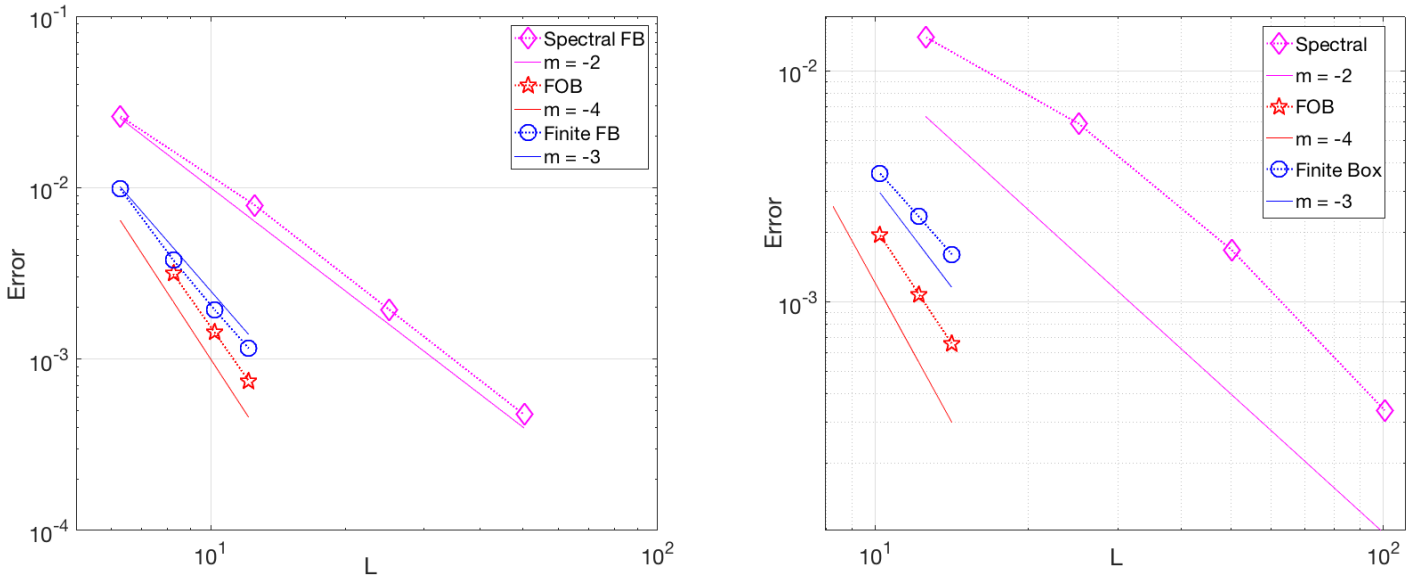

Figure 15. Left: convergence results for temperature at laser source in a square domain with side length L. Right: convergence results for intensity at distance 100 in a square domain with side length L. Error is Cauchy error measured between domain length iterations.

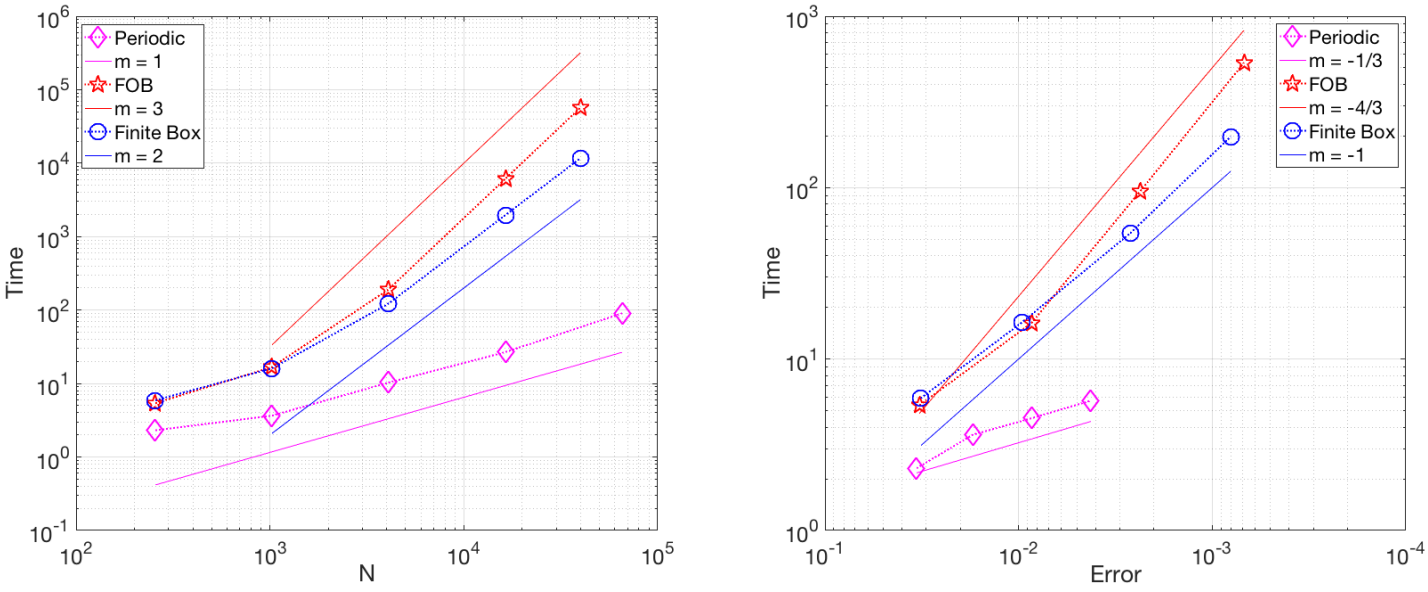

Figure 16. Left: computation times as a function of number of grid points in the domain, N, using fixed square domain size with length on a side $L = 2\pi + 1$ while number of points is increased by powers of 2. Right: computation times as a function of Cauchy error measured for varying domain size, L; note that the Error axis is flipped so that error decreases from left to right. Simulation timing was performed on a Mac Pro with 3.5 Ghz 6-core Intel Xeon E5 Processor.

V. Scintillation

5.1 Introduction

Scintillation arises from variations in intensity of a light source caused by phase distortions throughout space between the light source and the observer [81]. Phase distortions can be considered as atmospheric turbulence. Scintillation encompasses variations in time with respect to received irradiance [1]. This chapter is concerned with the temporal variation in received irradiance.

Scintillation is an essential part of the fluid-beam interaction. In addition, small amplitude changes exist independent of the laser, these cause scintillation. It is characterized by changes in the refractive index of the medium; these changes are caused almost exclusively by fluctuations in temperature [42, 56] as noted in the discussion of the refractive index in Section 2.3.

The small scale structure of the temperature distribution directly affects the scattering of the HEL beam [82], degrading the quality of electromagnetic beams in optical communications [42].

In this section we introduce a coupled solver which incorporates scintillation in order to simulate fluid-beam interaction, including small scale turbulence from both initial phase distortions in the temperature field and distortions induced by HEL beam heating.

Scintillation is incorporated asymptotically into the coupled fluid-beam model using a hybrid volumetric, phase screen methodology.

Generation and application of phase screens is a well documented area of research. Methods have been developed for efficiently generating phase screens [83, 84, 85, 86]. Several methods for creating highly accurate phase screens have been developed [28, 87, 88, 89, 90, 91, 92, 93, 94]. There are also several methods generating phase screens

with respect to structure functions [95], or thickness [96, 97] allowing for analysis of temporal phenomenon in laser beam propagation. None of these methods account for fluid heating effects on the beam intensity as well as the temperature phase.

Phase screens are generated by applying the Fast-Fourier transform (FFT) method, or spectral method, first set forth as a Fourier transform method in [98], and detailed as a FFT method in [99]. Lane et al. in [90] and Frehlich in [28] provide an improvement by accounting for subharmonics, thus incorporating lower spatial frequencies [39]. The covariance matrix method [83], while more accurate, requires computational costs too great for our iterative approach. In contrast to [84] and [96] the volumetric approach is applied with 2-D temperature screens evolved to proportional time-steps, as in the quiescent case, to account for temporal phenomena. To handle scintillation initial random temperature phase screens are simulated in linearized Boussinesq equations. This allows for a dynamic update of the beam intensity as the fluid is heated and convects over time. The details of this method are discussed in the following section.

5.2 Formulation

This section describes the asymptotic definition to incorporate scintillation effects into the fluid model (13). Recalling that initial conditions for the Boussinesq equations are:

$$\mathbf{u}(\mathbf{x}, 0) = 0$$

$$T(\mathbf{x}, 0) = T_0,$$

$$P(\mathbf{x}, 0) = 0$$

where $\mathbf{x} = \begin{bmatrix} x \\ y \\ z \end{bmatrix}$.

Scintillation can, therefore, be described asymptotically by

$$\mathbf{u}(\mathbf{x}, 0) = 0 + \delta \mathbf{u}_1$$

$$T(\mathbf{x}, 0) = T_0 + \delta T_1,$$

$$P(\mathbf{x}, 0) = 0 + \delta P_1$$

where $\delta \to 0$ so that it makes sense to write the solution as a power series

$$\mathbf{u}(\mathbf{x}, t) = \mathbf{u}_0 + \delta \mathbf{u}_1$$

$$T(\mathbf{x}, t) = T_0 + \delta T_1$$

$$P(\mathbf{x}, t) = P_0 + \delta P_1.$$

The terms $\mathbf{u}_0(\mathbf{x}, t)$, $\mathbf{u}_1(\mathbf{x}, t)$, $T_0(\mathbf{x}, t)$, $T_1(\mathbf{x}, t)$, $P_0(\mathbf{x}, t)$ and $P_1(\mathbf{x}, t)$ are all $O(1)$.

Substituting the asymptotic expansions just defined into Boussinesq gives the $O(1)$ equations

$$\frac{\partial \mathbf{u}_0}{\partial t} + (\mathbf{u}_0 \cdot \nabla)\, \mathbf{u}_0 = \nabla P_0 + \frac{1}{Re} \nabla^2 \mathbf{u}_0 + \frac{1}{Fr^2} T_0 \mathbf{e}_1$$

$$\frac{\partial T_0}{\partial t} + (\mathbf{u}_0 \cdot \nabla)\, T_0 = \frac{1}{Pe} \nabla^2 T_0 + St|A|^2.$$

Note that the convective derivatives have been explicitly spelled out since higher order equations apply a product rule in the convective derivative as in the $O(\delta)$ expansion:

$$\frac{\partial \mathbf{u}_1}{\partial t} + (\mathbf{u}_0 \cdot \nabla)\, \mathbf{u}_1 + (\mathbf{u}_1 \cdot \nabla)\, \mathbf{u}_0 = \nabla P_1 + \frac{1}{Re} \nabla^2 \mathbf{u}_1 + \frac{1}{Fr^2} T_1$$

$$\frac{\partial T_1}{\partial t} + (\mathbf{u}_0 \cdot \nabla) T_1 + (\mathbf{u}_1 \cdot \nabla) T_0 = \frac{1}{Pe} \nabla^2 T_1.$$

Initial data for the fluctuating term T_1 is determined by turbulent spectra; in order to satisfy the Boussinesq equations the turbulent spectra must be continuously differentiable. Moreover T_1 is an instance of a random process with power spectral density (PSD) $|\phi(f)|^2$. The simplest method to generate a phase spectrum is the Fast Fourier transform (FFT) method [90, 28, 39]:

$$T_1 = \phi(\kappa) e^{i\theta_\kappa} \tag{38}$$

where θ_κ is a random number, and κ is the scalar spatial wave number.

The following section describes the process of generating phase screens to be used as random turbulent spectra, T_1.

Random Phase Screen Generation.

Selecting a PSD for generating a temperature phase screen allows for some flexibility. Each PSD provides advantages of its own [100, 1]. Figure 17 shows a few turbulent spectra, illustrating the behavior of the turbulence as a function of wave number, κ.

A modified Von Kármán PSD was selected to generate T_1

$$|\phi(\kappa)|^2 = 0.033 C_n^2 \frac{\exp\left(-\kappa^2/\kappa_m^2\right)}{\left(\kappa^2 + \kappa_0^2\right)^{11/6}} \qquad \text{, for} \qquad 0 \leq \kappa < \infty, \tag{39}$$

where C_n^2 is the refractive index structure function, $\kappa_m = 5.93/l_0$ and $\kappa_0 = 2\pi/L_0$; l_o is the inner scale and L_0 is the outer scale of turbulence. Values of κ_m and κ_0 are selected to scale with the small-scale (high frequency) and large-scale (low frequency) behavior of the spectrum as determined by dimensional analysis [39]. Modified Von

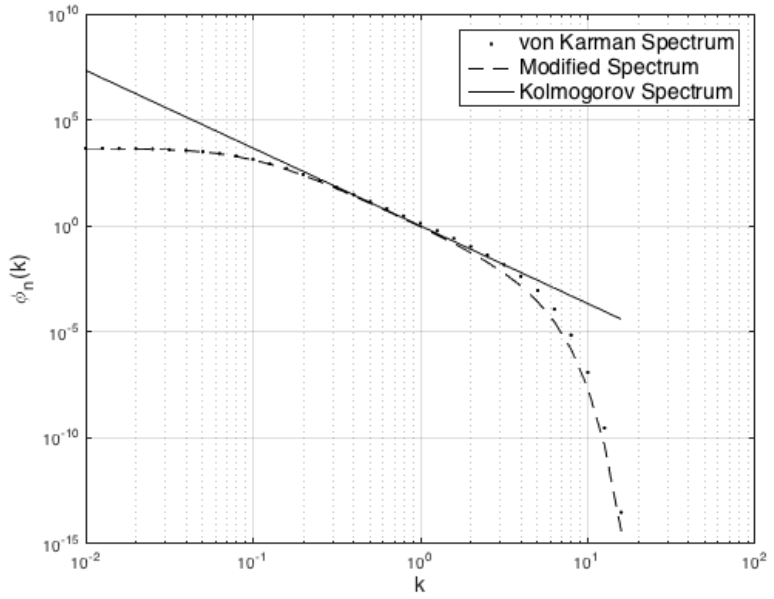

Figure 17. Plot of several turbulent spectra drawn from [1] illustrating the range of turbulent flow for an array of values of k; these spectra use $m = 11/3$ and $C_n^2 = 10^{-14}$.

Kármán was chosen for its accuracy and since it is the simplest model to incorporate inner-scale effects to the spectrum [100, 39].

The refractive index structure function, C_n^2, is a measure of local turbulence strength, which is frankly difficult to measure. There are measures with clearer meaning that are easier to come by. Moreover, C_n^2 is a function of propagation distance Δz so $C_n^2(z)$ can be used to compute atmospheric coherence diameter, r_0. Schmidt, in [39], transforms (39) to put it in terms of spatial frequency, r_0

$$|\phi(\kappa)|^2 = 0.4933 r_0^{-5/3} \frac{\exp\left(-\kappa^2/\kappa_m^2\right)}{\left(\kappa^2 + \kappa_0^2\right)^{11/6}}. \tag{40}$$

Phase screen generation is typically accomplished via weighted sums of basis functions. The most common basis sets are Zernike polynomials and Fourier series. The coupled laser-fluid solver already uses periodic boundary conditions therefore a Fourier series basis set makes sense. We apply the FFT method laid out by Schmidt

in [39], who bases his method on [98]. This method uses spatial frequency, f, rather than spatial wave number κ. Therefore (40) is expressed in terms of f

$$|\phi(f)|^2 = 0.023 r_0^{-5/3} \frac{\exp\left(-f^2/f_k^2\right)}{\left(f^2 + f_0^2\right)^{11/6}}, \tag{41}$$

where $f = \sqrt{f_m^2 + f_n^2}$, f_n and f_m are x and y-directed spatial frequencies, $f_k = (11.84\pi)/l_0$ and $f_0 = 1/L_0$ [39].

Phase screens are generated on a finite grid expressing T_1 as a Fourier series in a 2-dimensional plane expressing T_1 as a function of space variables x and y.

$$T_1(x, y) = \sum_{n=-\infty}^{\infty} \sum_{n=-\infty}^{\infty} c_{n,m} e^{i2\pi(f_n x + f_m y)},$$

where $c_{n,m}$ are the Fourier-series coefficients [39] .

In general, the Fourier coefficients are complex; the real and imaginary parts of $c_{n,m}$ have a Gaussian distribution with zero mean and equal variances with cross-variances equal to zero [1, 29, 30, 31, 39]. The variance is given by

$$\left\langle |c_{n,m}|^2 \right\rangle = \frac{1}{L_x L_y} |\phi(f)|^2 \tag{42}$$

where L_x and L_y are the x and y grid sizes respectively [39].

To implement random realizations of the Fourier-coefficients we use Matlab's randn function which provides random draws from the standard, normal Gaussian distribution. To transform the draws to the appropriate variance given in (42) multiply the random number by $\sqrt{\frac{1}{L_x L_y} |\phi(f)|^2)}$ [39]. The variance of the result decays as in (41).

The FFT method is not very accurate, and it has been shown in [28] that the subharmonic method described in [90] produces accurate results [39]. Therefore the

phase screen method in the scintillated coupled laser-fluid solver adds a subharmonics correction as in[39].

The next section describes how random phase screens are employed in the scintillated coupled solver.

Scintillation Model.

In order to incorporate scintillation into the coupled solver initialize $T_0(x, y, z) = 0$. $T_1(x, y, z)$ is initialized using the FFT method described in the previous section. A random realization of a temperature screen is shown in Figure 18. For each of T_0 and T_1 this process generates an independent array of N_z 2-dimensional arrays, where $N_z = L_z/\Delta z$ for propagation distance L_z.

The beam is evolved volumetrically as before using the Paraxial equation with $\eta_1(T_0)$ determining the refractive index. The beam profile is initialized with a Gaussian beam profile $A_0(x, y) = e^{-x^2-y^2}$. The beam is still evolved via linear interpolation by taking two-dimensional instances of T_0 two at a time. That is, the volumetric beam evolution of the Paraxial equation does not rely on phase screen creation; intensity A_t is output from the paraxial simulation. Scintillation is introduced as a phase screen at the end of each step in space, Δz, by

$$A_{t_2}(z + \Delta z) = A_t(z) \exp\left(i\delta T_1(z)\right).$$

Treating T as a constant we show the impact of δ on the beam intensity spot. As δ increases the beam spot appears more broken up into spots of higher, concentrated intensity and areas of lower intensity diffused throughout the spot. The Paraxial beam simulation was run at a distance of 800 and varied δ with constant fluid temperature. HEL beam intensity spots for varying δ are show in Figure 19. Since average intensity is conserved, maximum intensity actually increases as δ increases, the concentrated

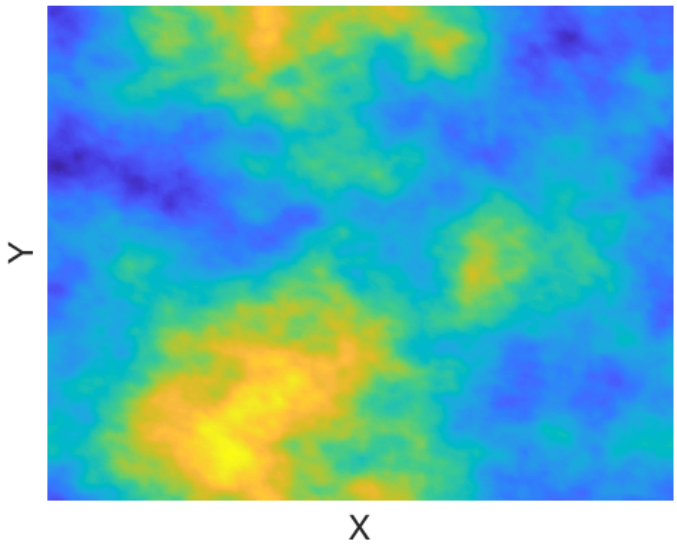

Figure 18. To illustrate $T_0(\mathbf{x}, 0)$ we show a random realization of a temperature phase screen. Generated via modified von Karman as described in Chapter V.

high intensity spots must reach higher values as lower intensity areas in the beam become more widespread.

Our coupled beam-fluid solver generates a constant fluid temperature initial beam profile in order to initialize the fluid solver. This intensity is passed to the linearized fluid solver.

Fluid velocity is initialized with $\mathbf{u}_0 = \mathbf{u}_1 = 0$; for fluid boundary conditions periodic boundary conditions are chosen for speed and resolution advantages. Periodic boundary conditions allow fast Fourier methods so that large numbers of points can be used to get higher resolution and lower error with a smaller computation cost.

At each slice the fluid is now evolved by linearized Boussinesq equations

$$\frac{\partial \mathbf{u}_0}{\partial t} + (\mathbf{u}_0 \cdot \nabla)\,\mathbf{u}_0 = \nabla P_0 + \frac{1}{Re}\nabla^2 \mathbf{u}_0 + \frac{1}{Fr^2} T_0 \mathbf{e}_1 \tag{43a}$$

$$\frac{\partial T_0}{\partial t} + (\mathbf{u}_0 \cdot \nabla)\,T_0 = \frac{1}{Pe}\nabla^2 T_0 + St|A|^2 \tag{43b}$$

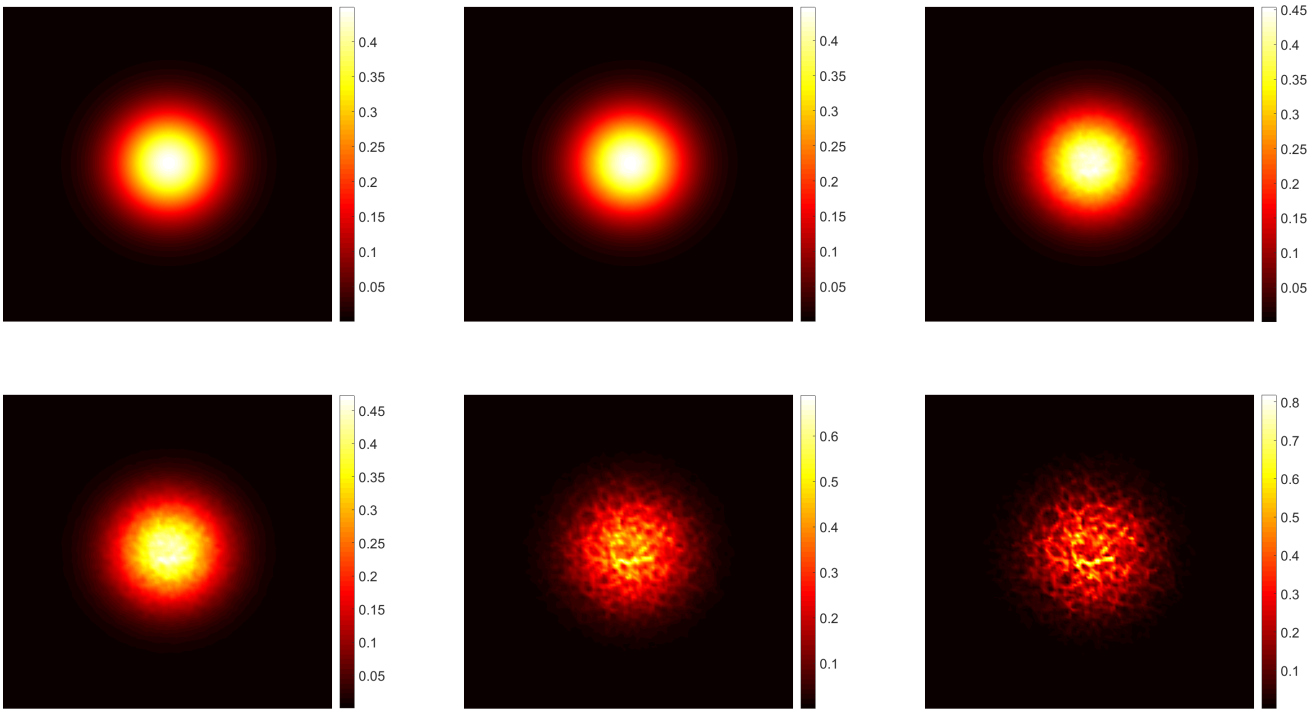

Figure 19. Top Row: Intensity beam spot with constant fluid temperature and $\delta = \{0, 0.01, 0.05\}$. Bottom Row: Intensity beam spot with constant fluid temperature, over propagation distance $L_z = 800$, using 20 screens and $\delta = \{0.1, 0.05, 1\}$. Scintillation impact on beam spot becomes clear for $\delta \geq 0.05$. Average intensity is preserved, we can therefore observe maximum beam intensity increase as δ increases.

$$\nabla \cdot \mathbf{u}_0 = 0. \tag{43c}$$

$$\frac{\partial \mathbf{u}_1}{\partial t} + (\mathbf{u}_0 \cdot \nabla)\,\mathbf{u}_1 + (\mathbf{u}_1 \cdot \nabla)\,\mathbf{u}_0 = \nabla P_1 + \frac{1}{Re}\nabla^2 \mathbf{u}_1 + \frac{1}{Fr^2} T_1 \tag{43d}$$

$$\frac{\partial T_1}{\partial t} + (\mathbf{u}_0 \cdot \nabla)\,T_1 + (\mathbf{u}_1 \cdot \nabla)\,T_0 = \frac{1}{Pe}\nabla^2 T_1 \tag{43e}$$

$$\nabla \cdot \mathbf{u}_1 = 0. \tag{43f}$$

The linearized optical fluid equations, (43), are numerically solved in Fourier space evolving through time using Runge-Kutta 4. A pressure correction scheme is applied a la [49]. The fluctuating small-scale variables $\mathbf{u}_1, T_1, P_1$ are forced by, and evolved along with, the base flow large-scale variables $\mathbf{u}_0, T_0, P_0$.

To evolve the fluid and beam together over a distance, L_z and over a time, t the predictor-corrector method is applied once again in the scintillated fluid-beam solver. Specifically the linearized fluid solver is first evolved for only a half time step in order to get a predicted fluid temperature fields, $T_{0,\Delta t/2}$ and $T_{1,\Delta t/2}$. $T_{0,\Delta t/2}$ is used in the Paraxial solver to evolve the beam through all of L_z volumetrically. $T_{1,\Delta t/2}$ is used as the phase screen to incorporate scintillation. The resulting intensity is used in the linearized fluid solver to provide corrected fluid temperature fields for the full time step, $T_{0,\Delta t}$ and $T_{1,\Delta t}$, which is used to correct the beam intensity in the Paraxial solver. $T_{0,\Delta t}$ is used in the Paraxial solver to evolve the beam through all of L_z volumetrically. $T_{1,\Delta t}$ is used as the phase screen to incorporate scintillation.

Results for various δ values are provided in the next section.

5.3 Results

Figure 20 shows stills from a video taken by Wick and Lloyd [2], and is provided as a point of comparison for the reader. The effects of convection induced by laser heating are illustrated in Figure 20. The beam spot deforms to a crescent, and is displaced by heating from the laser changing the index of refraction. Heating further induces scintillation which can be seen in the dark spots traveling through the laser spot as well as the overall blurring of the spot.

Simulations of scintillation show similar behavior in the simulated laser beam spot. The top row of Figure 21 shows three time slices evolved in the coupled laser-fluid solver with scintillation scaling factor $\delta = 10^{-6}$. The bottom row of Figure 21 shows fluid temperature evolved with the same settings. The non-dimensional constants are set to $St = \frac{1}{3}$, $Ri = 6 \times 10^5$, $Re = 1000$, and $Pe = 1000$. The laser is propagated over $L_z = 800$ for time $T_f = 0.6$.

Using the velocity and temperature values from the scintillated fluid-beam solver

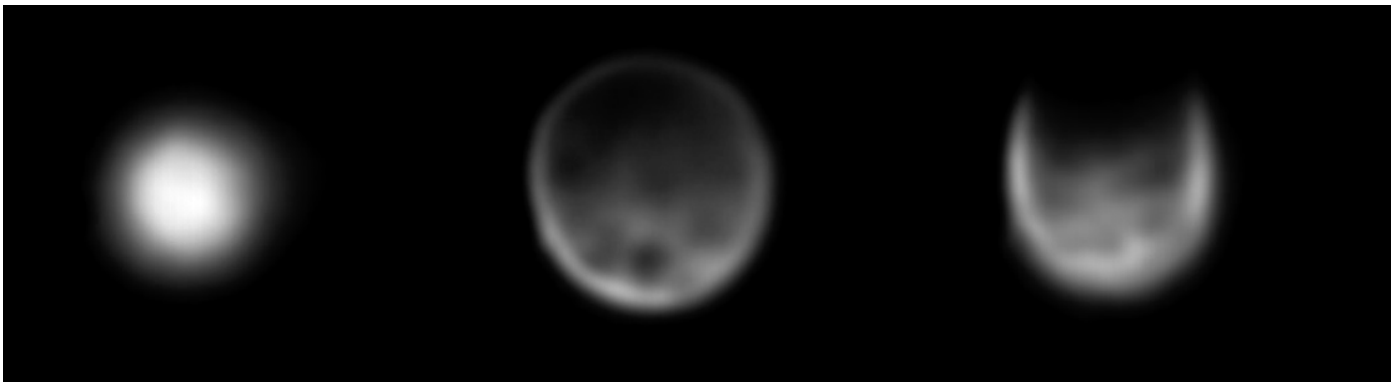

Figure 20. Still from a video of a 2.5 kW laser beam spot over path length 36", taken by Wick and Lloyd [2], propagated through smoke from burning oil and rubber. Stills taken, from left to right, at $t = 0$ sec, $t = 6$ sec and $t = 55$ sec. The effect of convection on the laser spot is clear from the crescent that forms in the beam spot, and the beam spot displacement. Scintillation is shown in the dark spots and the blurring of the laser spot

in (3) gives $C_T^2 = 1.38 \times 10^{-9} m^{-2/3}$. And using this C_T^2 in (2) gives $C_n^2 = 1.22 \times 10^{-16} m^{-2/3}$.

The scale factor in Figure 21 is too small to make an impact on the intensity spot. The beam deformation from convection is visible by $t = 0.2$.

The bottom row in Figure 21 shows the fluid temperature. The scale factor is too small to make an impact on the fluid temperature. The heated spot from the laser is visibly blooming by $t = 0.6$.

The top row of Figure 22 shows three time slices evolved in the coupled laser-fluid solver with scintillation scaling factor $\delta = 0.001$. The bottom row Figure 22 shows fluid temperature evolved with the same settings. The non-dimensional constants are set to $St = \frac{1}{3}$, $Ri = 6 \times 10^5$, $Re = 1000$, and $Pe = 1000$. The laser is propagated over $L_z = 800$ for time $T_f = 0.6$.

Using the velocity and temperature values from the scintillated fluid-beam solver in (3) gives $C_T^2 = 1.45 \times 10^{-7} m^{-2/3}$. And using this C_T^2 in (2) gives $C_n^2 = 1.27 \times 10^{-14} m^{-2/3}$.

The scale factor in Figure 22 introduces small scintillation to the beam spot. The

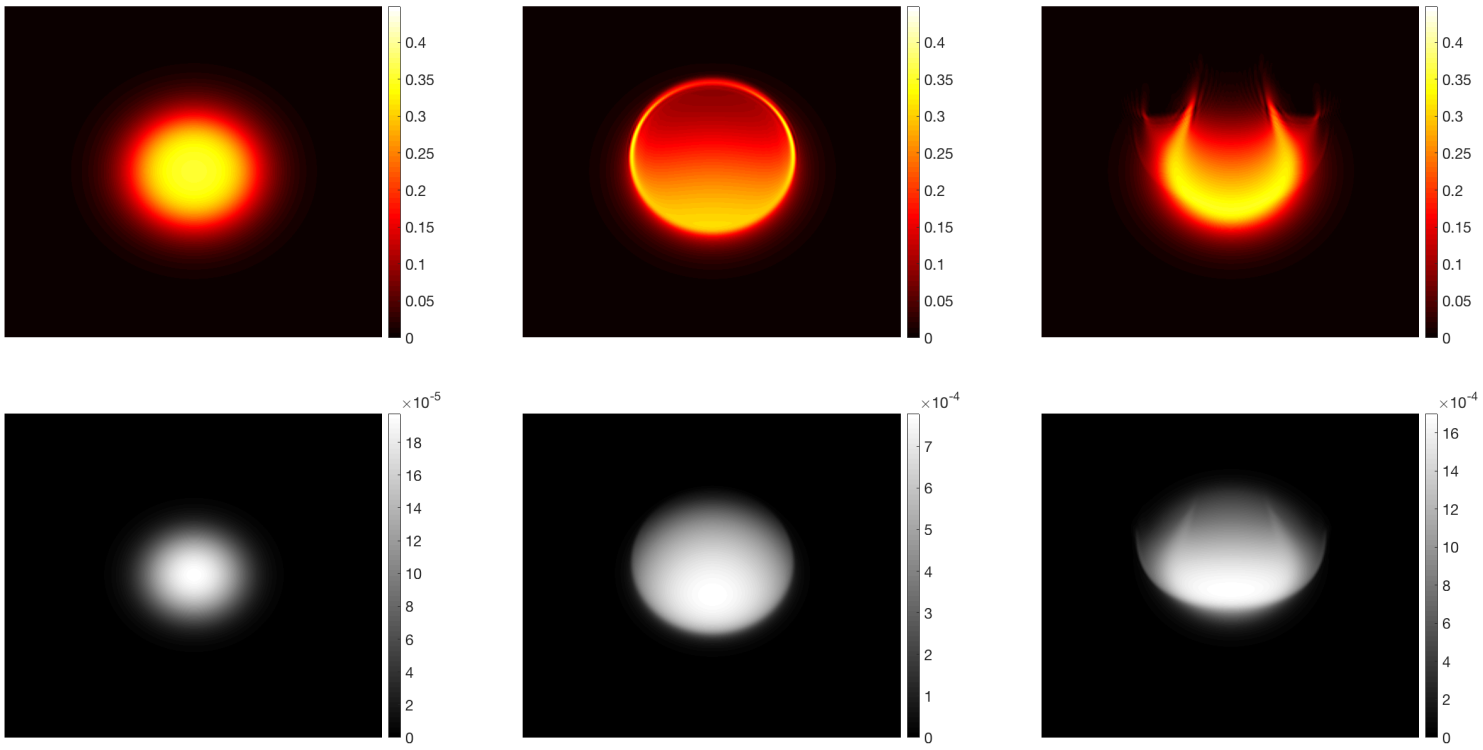

Figure 21. Top: Laser intensity beam spot generated by coupled laser-fluid solver with $\delta = 10^{-6}$. From left to right the spot is shown at $t = 0.0125$, $t = 0.2$, $t = 0.6$ Bottom: Fluid temperature spot generated by coupled laser-fluid solver with $\delta = 10^{-6}$. From left to right the spot is shown at $t = 0.0125$, $t = 0.2$, $t = 0.6$. Refractive index structure parameter value for this simulation is $C_n^2 = 1.22 \times 10^{-16} m^{-2/3}$

deformation of the beam spot is still visible. Slight blurring is visible with some lower intensity spots mixing into high intensity regions of the beam. The beam deformation from convection is visible by $t = 0.2$.

The bottom row of Figure 22 shows the corresponding fluid temperature. corresponding to the regime used to generate Figure 22. Fluid temperature is not affected by δ until $t = 0.6$, and then only small temperature differences are visible within the temperature spot.

The top row of Figure 23 shows three time slices evolved in the coupled laser-fluid solver with scintillation scaling factor $\delta = 0.01$. The bottom row of Figure 23 shows fluid temperature evolved with the same settings. The non-dimensional constants are

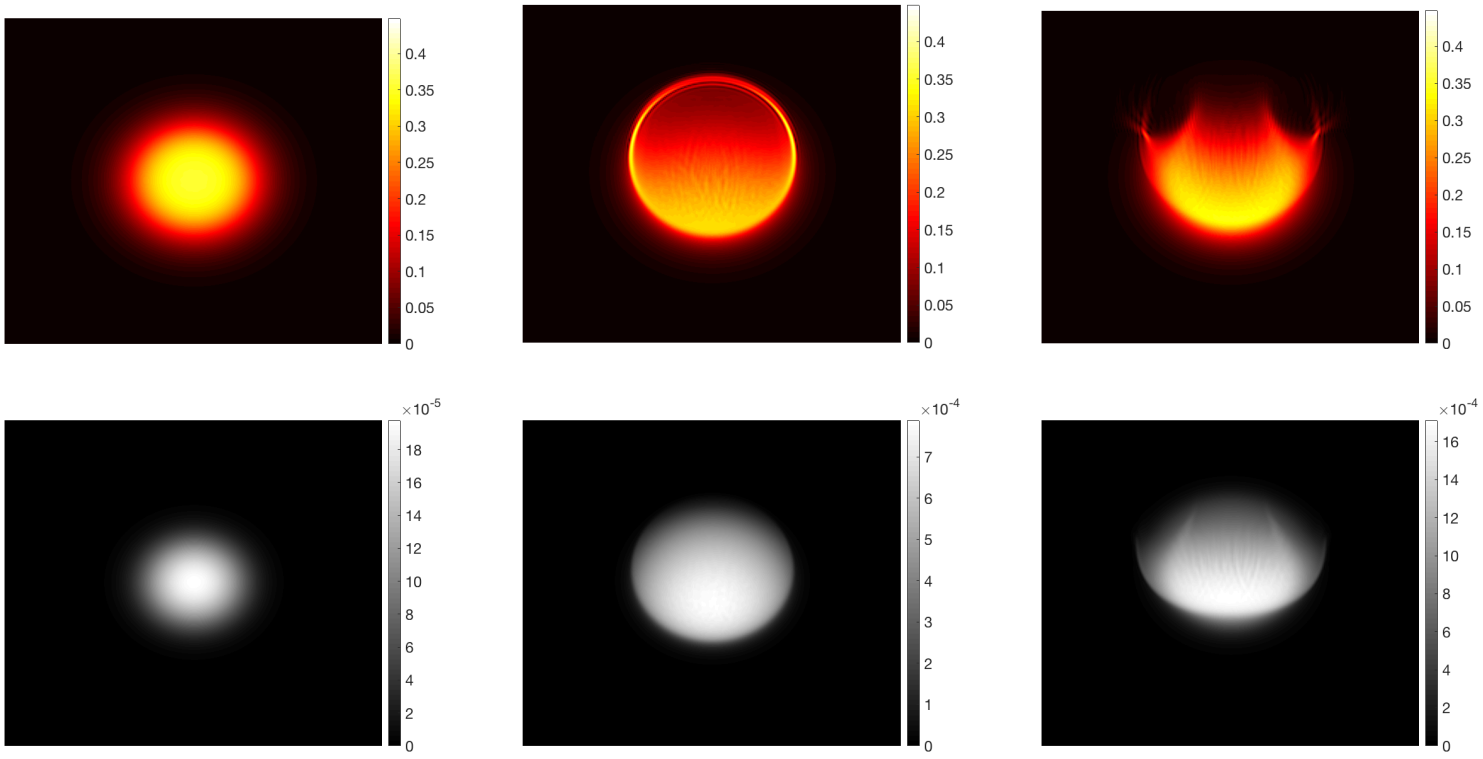

Figure 22. Top: Laser intensity beam spot generated by coupled laser-fluid solver with $\delta = 10^{-3}$. From left to right the spot is shown at $t = 0.0125$, $t = 0.2$, $t = 0.6$ Bottom: Fluid temperature spot generated by coupled laser-fluid solver with $\delta = 10^{-3}$. From left to right the spot is shown at $t = 0.0125$, $t = 0.2$, $t = 0.6$. Refractive index structure parameter value for this simulation is $C_n^2 = 1.27 \times 10^{-14} m^{-2/3}$

set to $St = \frac{1}{3}$, $Ri = 6 \times 10^5$, $Re = 1000$, and $Pe = 1000$. The laser is propagated over $L_z = 800$ for time $T_f = 0.6$.

Using the velocity and temperature values from the scintillated fluid-beam solver in (3) gives $C_T^2 = 7.73 \times 10^{-4} m^{-2/3}$. And using this C_T^2 in (2) gives $C_n^2 = 6.79 \times 10^{-11} m^{-2/3}$.

The value of $\delta = 0.01$ shows a strong influence of scintillation on the beam intensity spot. Definite spreading in the intensity is clear throughout the images in Figure 23. Deformation of the intensity spot due to self-induced convection is still visible by $t = 0.2$.

The bottom row of Figure 23 shows the corresponding fluid temperature. The

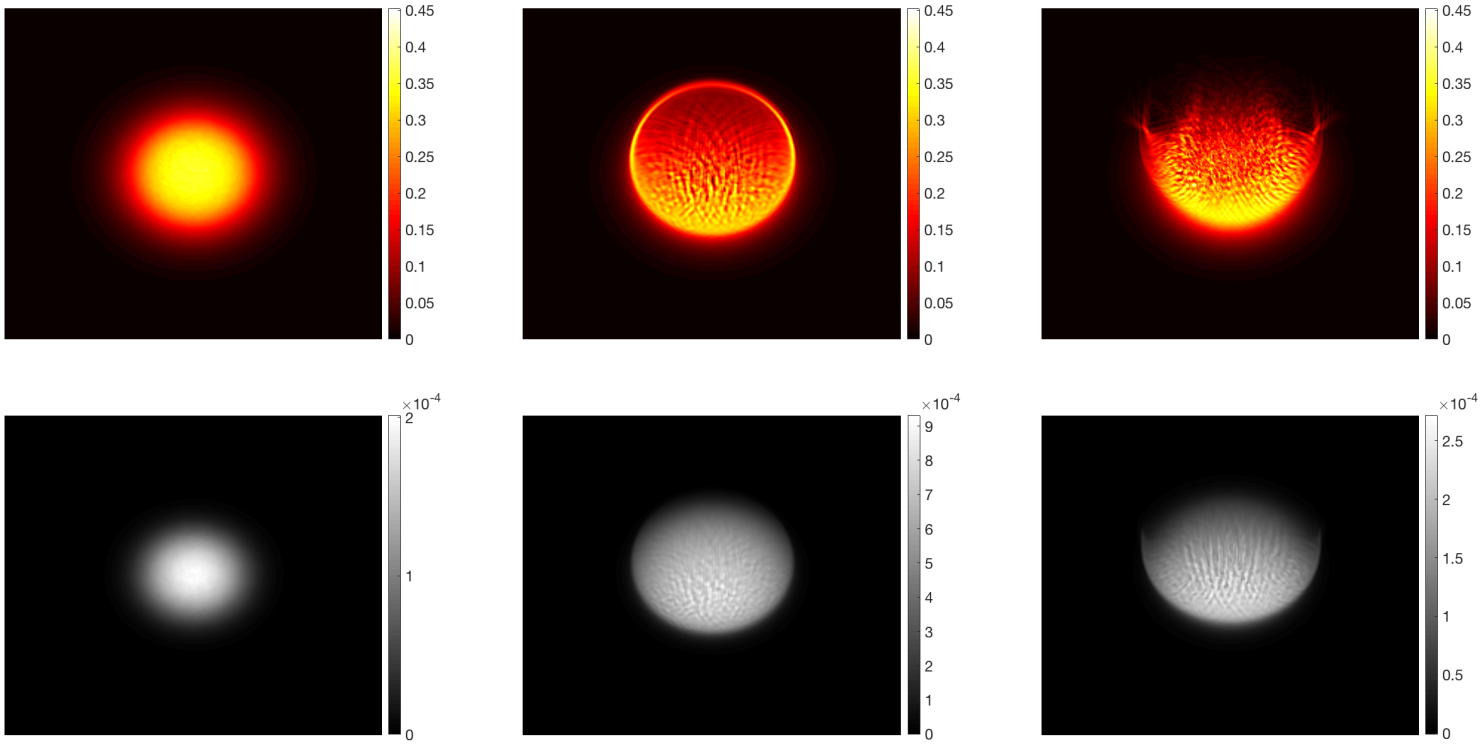

Figure 23. Top: Laser intensity beam spot generated by coupled laser-fluid solver with $\delta = 0.01$. From left to right the spot is shown at $t = 0.0125$, $t = 0.2$, $t = 0.6$ Bottom: Fluid temperature spot generated by coupled laser-fluid solver with $\delta = 0.01$. From left to right the spot is shown at $t = 0.0125$, $t = 0.2$, $t = 0.6$. Refractive index structure parameter value for this simulation is $C_n^2 = 6.79 \times 10^{-11} m^{-2/3}$

fluid temperature spot still has a similar shape in Figure 23 as the much lower δ shown in Figure 21. Though some spots of lower temperature are peppered through the temperature bloom.

The top row of Figure 24 shows three time slices evolved in the coupled laser-fluid solver with scintillation scaling factor $\delta = 0.06$. The bottom row of Figure 23 shows fluid temperature evolved with the same settings. The non-dimensional constants are set to $St = \frac{1}{3}$, $Ri = 6 \times 10^5$, $Re = 1000$, and $Pe = 1000$. The laser is propagated over $L_z = 800$ for time $T_f = 0.6$.

Using the velocity and temperature values from the scintillated fluid-beam solver in (3) gives $C_T^2 = 0.0079 m^{-2/3}$. And using this C_T^2 in (2) gives $C_n^2 = 6.91 \times 10^{-10} m^{-2/3}$.

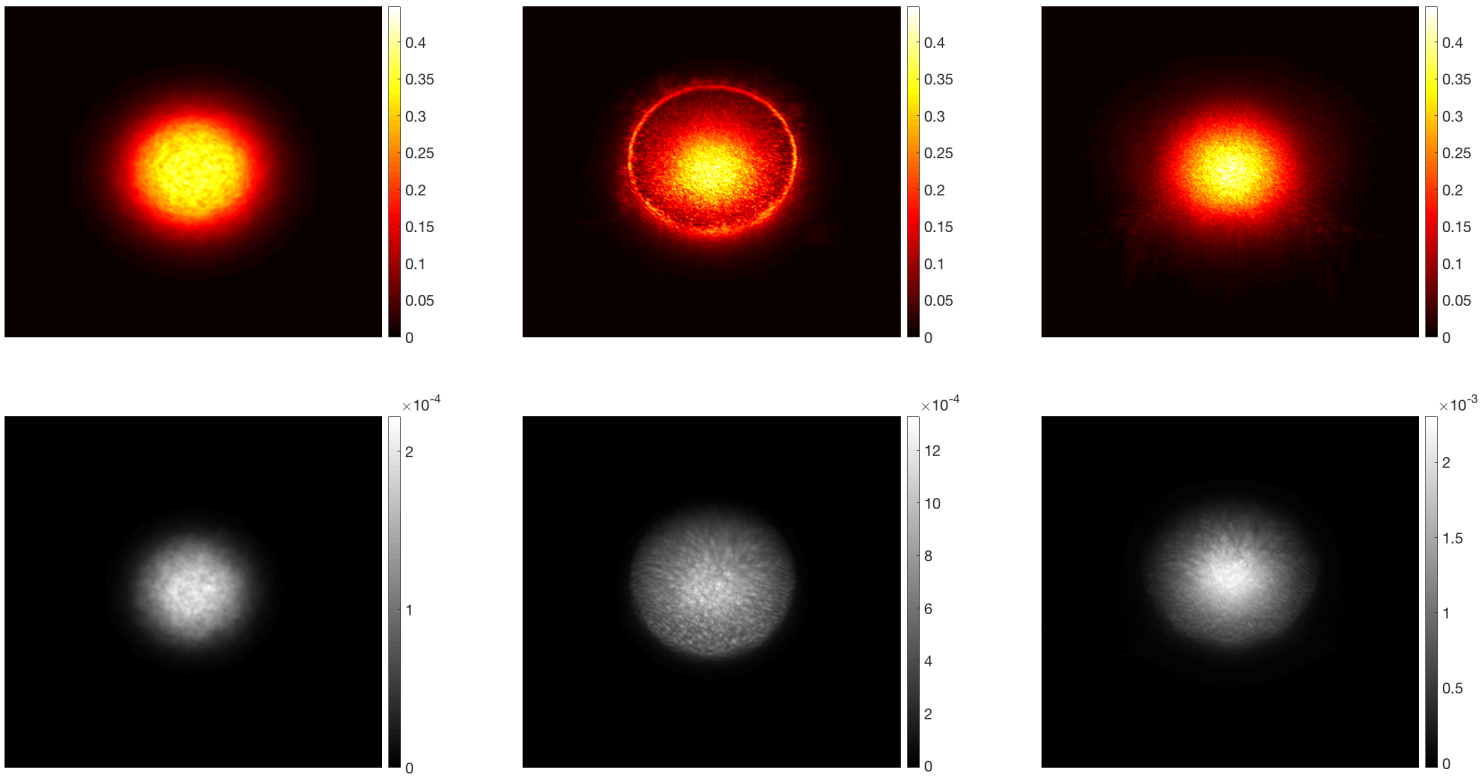

Figure 24. Top: Laser intensity beam spot generated by coupled laser-fluid solver with $\delta = 0.06$. From left to right the spot is shown at $t = 0.0125$, $t = 0.2$, $t = 0.6$ Bottom: Fluid temperature spot generated by coupled laser-fluid solver with $\delta = 0.06$. From left to right the spot is shown at $t = 0.0125$, $t = 0.2$, $t = 0.6$. Refractive index structure parameter value for this simulation is $C_n^2 = 6.91 \times 10^{-10} m^{-2/3}$

With $\delta = 0.06$ the scintillation overpowers convective effects on the beam intensity, as shown in Figure 24. The beam intensity shows ringing at $t = 0.2$ and by full time the beam spot shows fading but not much in the way of deformation as in less scintillated regimes.

The bottom row of Figure 24 shows the fluid temperature. Thermal blooming is less pronounced in Figure 24. With $\delta = 0.06$ some convection can be observed in a more diffuse low temperature spot. The temperature is spot is spread out with lower temperature on the outside of the spot with a concentrated high temperature spot in the middle.

The impact of the scintillation scale factor has been well demonstrated by the numerical results. Time constraints make a thorough study of the role of δ in scintillation difficult. Future work will involve obtaining video of lasers similar to the one shown in Figure 20. Comparing intensity spots in Figure 20 to simulated intensity spots in Figures 22 and 23 suggests that δ for Wick and Lloyd's experiment lies somewhere in the interval $(10^{-3}, 10^{-2})$. However the parameters of the experiment are necessary in order to describe the relationship between δ and parameters such as turbulence scale.

VI. Conclusions

A novel method for numerically modeling laser induced convection in its carrying medium was developed. Beam propagation was simulated volumetrically with FFT methods, and used interpolation between two-dimensional transverse temperature instances. Fluid dynamics were simulated with a predictor-corrector scheme, the Boussinesq model uses beam intensity from the Paraxial simulation to force temperature.

Boundary conditions for the free space problem were examined. The boundary conditions study provided a novel analysis of FOB. FOB provides an accurate, if costly, method for modeling laser propagation in an open environment. Imposing periodic boundary conditions is not as accurate, but access to FFT gives advantages in computation costs and allows for increased resolution in a reasonable amount of time. Therefore periodic boundary conditions were implemented in the scintillated coupled laser-fluid solver.

Scintillation was included in the coupled solver using a hybrid volumetric and phase-screen method. This is a computationally tractable method that allows inclusion of scintillation initially present in the media as well as dynamics. Asymptotically incorporating scintillation on intensity was shown to create distortion in the beam intensity. Behavior of the coupled solver was shown to parallel behavior of a laser experiment photographed by Wick and Lloyd. Comparison between the video and simulated intensity spots suggests that that δ for the experiment by Wick and Lloyd lies somewhere in the interval $(10^{-3}, 10^{-2})$. As scintillation was increased relative to laser power the turbulence of the fluid overcame the beam heating effects; the crescent shaped beam spot became, once more, a granular circular spot.

Future efforts in modeling scintillation in the coupled solver will focus on finding a relationship between the scintillation scaling factor δ and parameters like turbulence

scales. This can be accomplished by matching numerical results to experiments with known beam and atmospheric parameters.

6.1 Future Work

Figure 25 shows the laser beam end spot from the experiment in [2] next to two beam spots generated by the coupled solver using two different δ values. The experimental beam spot shows a degree of deformation and blurring somewhere between the numerically generated beam spots in Figure 25. It appears that δ for the experiment by Wick and Lloyd lies somewhere in the interval $(10^{-3}, 10^{-2})$. Future work in this area will include further matching simulations to laser experiments in order to determine a relationship between δ and scintillation parameters.

Decisions made for the fluid simulation in the coupled solver affected computation time and accuracy. The choice to use periodic boundary conditions so that the numerical solution to the fluid equation could be simulated more quickly means that the coupled solver actually uses the least accurate boundary conditions considered. Future work will investigate faster methods of employing FOB. Investigating Radial Basis Functions (RBF's) to drive down computation costs in FOB is an avenue of future work. RBF's allow us to use fewer points to get higher resolution since FOB does not need many points on the boundary leaving a lot of points for resolution in the immediate area about the beam.

The FOB conditions required constructing and inverting a matrix that was diagonal dominant. The matrix diagonal dominance is a direct result of decay of the basis set. This suggests an approximation to FOB using nearest neighbor methods. RBF-finite difference methods incorporate a nearest neighbor method where the basis function computes values only for a set number of points near the point being approximated. Future studies will look into applying this method in FOB to make

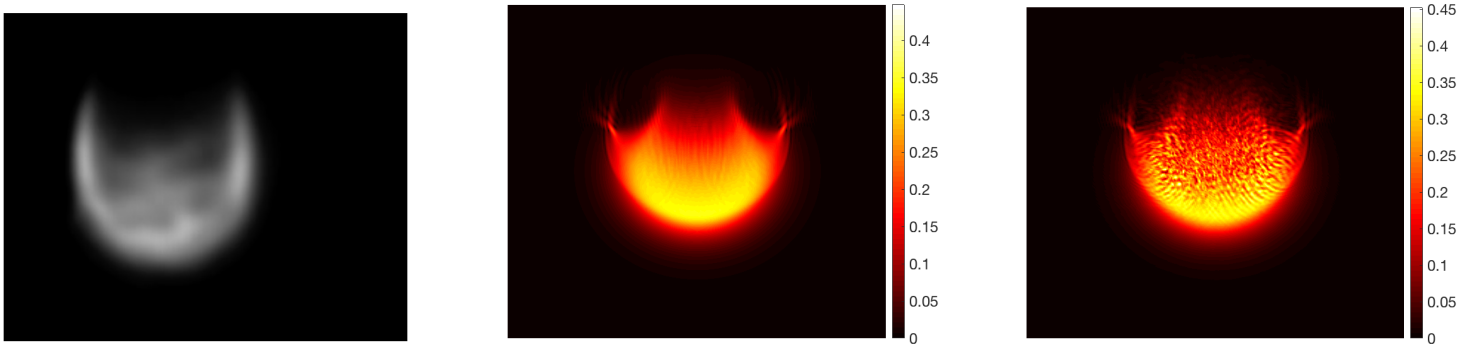

Figure 25. Wick experiment has apparent $\delta \in (10^{-3}, 10^{-2})$; middle and leftmost pictures are generated from coupled solver with $\delta = 10^{-3}$ and $\delta = 10^{-2}$ respectively. Finding δ values for experimental results is an avenue for future research.

applying fast inversion techniques possible.

The finite difference solver for fluid dynamics bears further investigation as well. There are fast poisson solvers that can be brought to bear to bring down the computation time [101, 102] of the finite difference solver since the solution to (16) takes the most time to compute. Reducing computation time for our simulation was not the focus of this study, but a comparison of coupled solver performance could be made using fast Poisson solvers in the fluid solver.

Bibliography

1. L. C. Andrews and R. L. Phillips, *Laser beam propagation through random media*, vol. 1. SPIE press Bellingham, WA, 2005.

2. P. Wick and C. Lloyd, "Blooming video." Taken at Naval Surface Warfare Center - Dahlgren Division, 2010. Video recieved via email from Steve Fiorino on 30 March 2018.

3. F. G. Gebhardt, "Twenty-five years of thermal blooming: an overview," in *OE/LASE'90, 14-19 Jan., Los Angeles, CA*, pp. 2–25, International Society for Optics and Photonics, 1990.

4. S. Sheldon, L. Knight, and J. Thorne, "Laser-induced thermal lens effect: a new theoretical model," *Applied optics*, vol. 21, no. 9, pp. 1663–1669, 1982.

5. D. C. Smith, "High-power laser propagation: thermal blooming," *Proceedings of the IEEE*, vol. 65, no. 12, pp. 1679–1714, 1977.

6. D. Carroll, "Overview of high energy lasers: Past, present, and future?," in *42nd AIAA Plasmadynamics and Lasers Conference in conjunction with the 18th International Conference on MHD Energy Conversion (ICMHD)*, p. 3102, 2011.

7. M. Perry, D. Pennington, B. Stuart, G. Tietbohl, J. Britten, C. Brown, S. Herman, B. Golick, M. Kartz, J. Miller, *et al.*, "Petawatt laser pulses," *Optics Letters*, vol. 24, no. 3, pp. 160–162, 1999.

8. Y. Sentoku, T. Liseikina, T. Z. Esirkepov, F. Califano, N. Naumova, Y. Ueshima, V. Vshivkov, Y. Kato, K. Mima, K. Nishihara, *et al.*, "High density collimated

beams of relativistic ions produced by petawatt laser pulses in plasmas," *Physical Review E*, vol. 62, no. 5, p. 7271, 2000.

9. C. Phipps, "Laser applications overview: the state of the art and the future trend in the united states," *RIKEN REVIEW*, pp. 11–19, 2003.

10. K. Liou, S.-C. Ou, Y. Takano, and J. Cetola, "Remote sensing of three-dimensional cirrus clouds from satellites: application to continuous-wave laser atmospheric transmission and backscattering," *Applied optics*, vol. 45, no. 26, pp. 6849–6859, 2006.

11. A. Wehr and U. Lohr, "Airborne laser scanning?an introduction and overview," *ISPRS Journal of photogrammetry and remote sensing*, vol. 54, no. 2, pp. 68–82, 1999.

12. D. E. Raible, D. Dinca, and T. H. Nayfeh, "Optical frequency optimization of a high intensity laser power beaming system utilizing vmj photovoltaic cells," in *Space Optical Systems and Applications (ICSOS), 2011 International Conference on*, pp. 232–238, IEEE, 2011.

13. L. Xie, Y. Shi, Y. T. Hou, and A. Lou, "Wireless power transfer and applications to sensor networks," *IEEE Wireless Communications*, vol. 20, no. 4, pp. 140–145, 2013.

14. N. Wang, Y. Zhu, W. Wei, J. Chen, S. Liu, P. Li, and Y. Wen, "One-to-multipoint laser remote power supply system for wireless sensor networks," *IEEE Sensors Journal*, vol. 12, no. 2, pp. 389–396, 2012.

15. F. G. Gebhardt, "Atmospheric effects modeling for high-energy laser systems,"

16. B. Fornberg, "Steady viscous flow past a circular cylinder up to reynolds number 600," *Journal of Computational Physics*, vol. 61, no. 2, pp. 297–320, 1985.

17. J. Gordon, R. Leite, R. Moore, S. Porto, and J. Whinnery, "Long-transient effects in lasers with inserted liquid samples," *Journal of Applied Physics*, vol. 36, no. 1, pp. 3–8, 1965.

18. J. Whinnery, D. Miller, and F. Dabby, "Thermal convention and spherical aberration distortion of laser beams in low-loss liquids," *IEEE Journal of Quantum Electronics*, vol. 3, no. 9, pp. 382–383, 1967.

19. F. G. Gebhardt and D. C. Smith, "Effects of wind on thermal defocusing of co2 laser radiation," *Applied Physics Letters*, vol. 14, no. 2, pp. 52–54, 1969.

20. F. Gebhardt and D. Smith, "Effects of diffraction on the self-induced thermal distortion of a laser beam in a cross-wind," *IEEE Journal of Quantum Electronics*, vol. 7, no. 6, pp. 274–275, 1971.

21. F. G. Gebhardt, "Self-induced thermal distortion effects on target image quality," *Applied optics*, vol. 11, no. 6, pp. 1419–1423, 1972.

22. F. Gebhardt and D. Smith, "Self-induced thermal distortion in the near field for a laser beam in a moving medium," *IEEE Journal of Quantum Electronics*, vol. 7, no. 2, pp. 63–73, 1971.

23. F. G. Gebhardt, "Airborne laser blooming and turbulence simulations," in *OE/LASE'94*, pp. 76–86, International Society for Optics and Photonics, 1994.

24. D. Smith, "Thermal defocusing of co 2 laser radiation in gases," *IEEE Journal of Quantum Electronics*, vol. 5, no. 12, pp. 600–607, 1969.

25. J. N. Hayes, "Thermal blooming of laser beams in fluids," *Applied optics*, vol. 11, no. 2, pp. 455–461, 1972.

26. J. Fleck, J. Morris, and M. Feit, "Time-dependent propagation of high energy laser beams through the atmosphere," *Applied Physics A: Materials Science & Processing*, vol. 10, no. 2, pp. 129–160, 1976.

27. J. F. Schonfeld, "The theory of compensated laser propagation through strong thermal blooming," *Lincoln Laboratory Journal*, vol. 5, pp. 131–150, 1992.

28. R. Frehlich, "Simulation of laser propagation in a turbulent atmosphere," *Applied Optics*, vol. 39, no. 3, pp. 393–397, 2000.

29. J. Recolons and F. Dios, "Accurate calculation of phase screens for the modeling of laser beam propagation through atmospheric turbulence," in *Proc. SPIE*, vol. 5891, pp. 51–62, 2005.

30. J. D. Strasburg and W. W. Harper, "Impact of atmospheric turbulence on beam propagation," in *Defense and Security*, pp. 93–102, International Society for Optics and Photonics, 2004.

31. S. A. C. Baluyot and N. P. Hermosa II, "Intensity profiles and propagation of optical beams with bored helical phase," *Optics express*, vol. 17, no. 18, pp. 16244–16254, 2009.

32. R. L. Fante, "Electromagnetic beam propagation in turbulent media: an update," *Proceedings of the IEEE*, vol. 68, no. 11, pp. 1424–1443, 1980.

33. T. H. Pries, "Atmospheric sensitivities of high energy lasers," tech. rep., DTIC Document, 1980.

34. M. D. Plourde, "Limitations of segmented wavefront control devices in emulating optical turbulence," tech. rep., Air Force Institute of Technology Wright-Patterson AFB OH School of Engineeering, 2008.

35. F. G. Gebhardt, "High power laser propagation," *Applied Optics*, vol. 15, no. 6, pp. 1479–1493, 1976.

36. S. Fiorino, R. Bartell, G. Perram, D. Bunch, L. Gravley, C. Rice, Z. Manning, M. Krizo, J. Roadcap, and G. Jumper, "The heleeos atmospheric effects package: A probabilistic method for evaluating uncertainty in low-altitude, high-energy laser effectiveness," *Journal of Directed Energy [JDE] JDE*, vol. 26, no. 17, p. 47, 2006.

37. D. Rohmistrov, A. Y. Bogushevich, and I. Botygin, "Methods and algorithms for statistical processing of instantaneous meteorological parameters from ultrasonic measurements," in *IOP Conference Series: Earth and Environmental Science*, vol. 48, p. 012031, IOP Publishing, 2016.

38. T. Manzur, J. Zeller, and E. Magee, "Near-marine boundary layer atmospheric and turbulence measurement and modeling," in *SPIE Defense, Security, and Sensing*, pp. 871117–871117, International Society for Optics and Photonics, 2013.

39. J. D. Schmidt, "Numerical simulation of optical wave propagation with examples in matlab," SPIE Bellingham, Washington, USA, 2010.

40. D. J. Tritton, *Physical fluid dynamics*. Springer Science & Business Media, 2012.

41. A. J. Chorin, "Numerical solution of the navier-stokes equations," *Mathematics of computation*, vol. 22, no. 104, pp. 745–762, 1968.

42. P. E. Raj, S. Sharma, P. Devara, and G. Pandithurai, "Study of laser scintillation in different atmospheric conditions," *Journal of Applied Meteorology*, vol. 32, no. 6, pp. 1161–1167, 1993.

43. R. S. Lawrence and J. W. Strohbehn, "A survey of clear-air propagation effects relevant to optical communications," *Proceedings of the IEEE*, vol. 58, no. 10, pp. 1523–1545, 1970.

44. P. Sprangle, J. Penano, and B. Hafizi, "Propagation of intense short laser pulses in the atmosphere," *Physical Review E*, vol. 66, no. 4, p. 046418, 2002.

45. P. Sprangle, J. Peñano, A. Ting, and B. Hafizi, "Propagation of high-energy lasers in a maritime atmosphere," *Naval Research Labs*, 2004.

46. J. R. Penano, P. Sprangle, and B. Hafizi, "Propagation of high energy laser beams through atmospheric stagnation zones," tech. rep., DTIC Document, 2006.

47. Y. E. Geints, G. Grachev, A. Zemlyanov, A. Kabanov, A. Pavlov, A. Ponomarenko, and V. Tishchenko, "Thermal self-action of high-power continuous and pulse-periodic co2 laser radiation in air: I. numerical simulation of propagation along an atmospheric path," *Atmospheric and Oceanic Optics*, vol. 27, no. 2, pp. 107–114, 2014.

48. W. Shyy, S. Thakur, and J. Wright, "Second-order upwind and central difference schemes for recirculatingflow computation," *AIAA journal*, vol. 30, no. 4, pp. 923–932, 1992.

49. B. F. Akers and J. A. Reeger, "Thermal blooming with laser-induced convection," *Pre-Publication*, 2018.

50. J. Bell, J. Solomon, and W. Szymczak, "A second-order projection method for the incompressible navier stokes equations on quadrilateral grids," in *9th Computational Fluid Dynamics Conference*, p. 1967, 1989.

51. D. L. Brown, R. Cortez, and M. L. Minion, "Accurate projection methods for the incompressible navier–stokes equations," *Journal of computational physics*, vol. 168, no. 2, pp. 464–499, 2001.

52. G. Taylor and A. Green, "Mechanism of the production of small eddies from large ones," *Proceedings of the Royal Society of London. Series A, Mathematical and Physical Sciences*, vol. 158, no. 895, pp. 499–521, 1937.

53. P. E. Ciddor, "Refractive index of air: new equations for the visible and near infrared," *Applied optics*, vol. 35, no. 9, pp. 1566–1573, 1996.

54. P. Sprangle, J. Penano, and B. Hafizi, "Optimum wavelength and power for efficient laser propagation in various atmospheric environments," tech. rep., DTIC Document, 2005.

55. J. Mandarino, "The gladstone-dale relationship; part i, derivation of new constants," *The Canadian Mineralogist*, vol. 14, no. 4, pp. 498–502, 1976.

56. J. W. Strohbehn, "Line-of-sight wave propagation through the turbulent atmosphere," *Proceedings of the IEEE*, vol. 56, no. 8, pp. 1301–1318, 1968.

57. R. L. Sani and P. M. Gresho, "Résumé and remarks on the open boundary condition minisymposium," *International Journal for Numerical Methods in Fluids*, vol. 18, no. 10, pp. 983–1008, 1994.

58. P. M. Gresho, "Incompressible fluid dynamics: some fundamental formulation issues," *Annual review of fluid mechanics*, vol. 23, no. 1, pp. 413–453, 1991.

59. S. Dong, "A convective-like energy-stable open boundary condition for simulations of incompressible flows," *Journal of Computational Physics*, vol. 302, pp. 300–328, 2015.

60. D. K. Gartling, "A test problem for outflow boundary conditions?flow over a backward-facing step," *International Journal for Numerical Methods in Fluids*, vol. 11, no. 7, pp. 953–967, 1990.

61. M. S. Engelman and M.-A. Jamnia, "Transient flow past a circular cylinder: a benchmark solution," *International Journal for Numerical Methods in Fluids*, vol. 11, no. 7, pp. 985–1000, 1990.

62. J. M. Leone, "Open boundary condition symposium benchmark solution: Stratified flow over a backward-facing step," *International Journal for Numerical Methods in Fluids*, vol. 11, no. 7, pp. 969–984, 1990.

63. M. Behr, J. Liou, R. Shih, and T. Tezduyar, "Vorticity-streamfunction formulation of unsteady incompressible flow past a cylinder: Sensitivity of the computed flow field to the location of the outflow boundary," *International Journal for Numerical Methods in Fluids*, vol. 12, no. 4, pp. 323–342, 1991.

64. J.-L. Guermond, P. Minev, and J. Shen, "Error analysis of pressure-correction schemes for the time-dependent stokes equations with open boundary conditions," *SIAM Journal on Numerical Analysis*, vol. 43, no. 1, pp. 239–258, 2005.

65. J. Liu, "Open and traction boundary conditions for the incompressible navier–stokes equations," *Journal of Computational Physics*, vol. 228, no. 19, pp. 7250–7267, 2009.

66. A. Sommerfeld, *Partial differential equations in physics*, vol. 1. Academic press, 1949.

67. I. Orlanski, "A simple boundary condition for unbounded hyperbolic flows," *Journal of computational physics*, vol. 21, no. 3, pp. 251–269, 1976.

68. J. Keskar and D. Lyn, "Computations of a laminar backward-facing step flow at re= 800 with a spectral domain decomposition method," *International journal for numerical methods in fluids*, vol. 29, no. 4, pp. 411–427, 1999.

69. M. Ol'Shanskii and V. M. Staroverov, "On simulation of outflow boundary conditions in finite difference calculations for incompressible fluid," *International Journal for Numerical Methods in Fluids*, vol. 33, no. 4, pp. 499–534, 2000.

70. M. Forestier, R. Pasquetti, R. Peyret, and C. Sabbah, "Spatial development of wakes using a spectral multi-domain method," *Applied numerical mathematics*, vol. 33, no. 1-4, pp. 207–216, 2000.

71. J. Craske and M. van Reeuwijk, "Robust and accurate open boundary conditions for incompressible turbulent jets and plumes," *Computers & Fluids*, vol. 86, pp. 284–297, 2013.

72. M. Ruith, P. Chen, and E. Meiburg, "Development of boundary conditions for direct numerical simulations of three-dimensional vortex breakdown phenomena in semi-infinite domains," *Computers & fluids*, vol. 33, no. 9, pp. 1225–1250, 2004.

73. C. Taylor, J. Rance, and J. Medwell, "A note on the imposition of traction boundary conditions when using the fem for solving incompressible flow problems," *International Journal for Numerical Methods in Biomedical Engineering*, vol. 1, no. 3, pp. 113–121, 1985.

74. J. Larsen and H. Dancy, "Open boundaries in short wave simulations?a new approach," *Coastal Engineering*, vol. 7, no. 3, pp. 285–297, 1983.

75. G. Jin and M. Braza, "A nonreflecting outlet boundary condition for incompressible unsteady navier-stokes calculations," *Journal of Computational Physics*, vol. 107, no. 2, pp. 239–253, 1993.

76. S. V. Tsynkov, "Numerical solution of problems on unbounded domains. a review," *Applied Numerical Mathematics*, vol. 27, no. 4, pp. 465–532, 1998.

77. Y. Zhou and Z. Wang, "Absorbing boundary conditions for the euler and navier–stokes equations with the spectral difference method," *Journal of Computational Physics*, vol. 229, no. 23, pp. 8733–8749, 2010.

78. D. Zhang, F. MA, and M. FANG, "Finite element method with perfectly matched absorbing layers for wave scattering from a cavity," *Chinese Journal of Computational Physics*, vol. 3, p. 008, 2008.

79. F. Nataf, "An open boundary condition for the computation of the steady incompressible navier-stokes equations," *Journal of Computational Physics*, vol. 85, no. 1, pp. 104–129, 1989.

80. B. Fornberg, "Steady viscous flow past a sphere at high reynolds numbers," *Journal of Fluid Mechanics*, vol. 190, pp. 471–489, 1988.

81. G. P. Perram, S. J. Cusumano, S. T. Fiorino, and R. L. Hengehold, *An introduction to laser weapon systems*. Directed Energy Professional Society, 2010.

82. G. K. Batchelor, "Small-scale variation of convected quantities like temperature in turbulent fluid part 1. general discussion and the case of small conductivity," *Journal of Fluid Mechanics*, vol. 5, no. 1, pp. 113–133, 1959.

83. C. M. Harding, R. A. Johnston, and R. G. Lane, "Fast simulation of a kolmogorov phase screen," *Applied optics*, vol. 38, no. 11, pp. 2161–2170, 1999.

84. F. Assémat, R. W. Wilson, and E. Gendron, "Method for simulating infinitely long and non stationary phase screens with optimized memory storage," *Optics express*, vol. 14, no. 3, pp. 988–999, 2006.

85. A. Beghi, A. Cenedese, and A. Masiero, "Stochastic realization approach to the efficient simulation of phase screens," *JOSA A*, vol. 25, no. 2, pp. 515–525, 2008.

86. V. Sriram and D. Kearney, "An ultra fast kolmogorov phase screen generator suitable for parallel implementation," *Optics express*, vol. 15, no. 21, pp. 13709–13714, 2007.

87. M. C. Roggemann, B. M. Welsh, and B. R. Hunt, *Imaging through turbulence*. CRC press, 1996.

88. G. Cochran, "Phase screen generation," *Tech. Rep. TR-663*, 1985.

89. B. J. Herman and L. A. Strugala, "Method for inclusion of low-frequency contributions in numerical representation of atmospheric turbulence," in *Propagation of High-Energy Laser Beams through the Earth's Atmosphere*, vol. 1221, pp. 183–193, International Society for Optics and Photonics, 1990.

90. R. Lane, A. Glindemann, J. Dainty, *et al.*, "Simulation of a kolmogorov phase screen," *Waves in random media*, vol. 2, no. 3, pp. 209–224, 1992.

91. H. Jakobsson, "Simulations of time series of atmospherically distorted wave fronts," *Applied optics*, vol. 35, no. 9, pp. 1561–1565, 1996.

92. B. M. Welsh, "Fourier-series-based atmospheric phase screen generator for simulating anisoplanatic geometries and temporal evolution," in *Propagation and Imaging through the Atmosphere*, vol. 3125, pp. 327–339, International Society for Optics and Photonics, 1997.

93. G. Sedmak, "Performance analysis of and compensation for aspect-ratio effects of fast-fourier-transform-based simulations of large atmospheric wave fronts," *Applied optics*, vol. 37, no. 21, pp. 4605–4613, 1998.

94. R. J. Eckert and M. E. Goda, "Polar phase screens: a comparative analysis with other methods of random phase screen generation," in *Atmospheric Optical Modeling, Measurement, and Simulation II*, vol. 6303, p. 630301, International Society for Optics and Photonics, 2006.

95. D. Kouznetsov, V. Voitsekhovich, and R. Ortega-Martinez, "Simulations of turbulence-induced phase and log-amplitude distortions," *Applied optics*, vol. 36, no. 2, pp. 464–469, 1997.

96. F. Dios, J. Recolons, A. Rodríguez, and O. Batet, "Temporal analysis of laser beam propagation in the atmosphere using computer-generated long phase screens," *Optics express*, vol. 16, no. 3, pp. 2206–2220, 2008.

97. D. L. Fried and T. Clark, "Extruding kolmogorov-type phase screen ribbons," *JOSA A*, vol. 25, no. 2, pp. 463–468, 2008.

98. B. L. McGlamery, "Restoration of turbulence-degraded images," *JOSA*, vol. 57, no. 3, pp. 293–297, 1967.

99. C. Macaskill and T. Ewart, "Computer simulation of two-dimensional random wave propagation," *IMA journal of applied mathematics*, vol. 33, no. 1, pp. 1–15, 1984.

100. L. C. Andrews, R. L. Phillips, and C. Y. Hopen, *Laser beam scintillation with applications*, vol. 99. SPIE press, 2001.

101. A. R. Abdullah, "The four point explicit decoupled group (edg) method: A fast poisson solver," *International Journal of Computer Mathematics*, vol. 38, no. 1-2, pp. 61–70, 1991.

102. T. F. Chan and D. C. Resasco, "A domain-decomposed fast poisson solver on a rectangle," *SIAM journal on scientific and statistical computing*, vol. 8, no. 1, pp. s14–s26, 1987.

REPORT DOCUMENTATION PAGE

Form Approved
OMB No. 0704–0188

1. REPORT DATE *(DD–MM–YYYY)*	2. REPORT TYPE	3. DATES COVERED *(From — To)*
09 – 2018	Doctoral Dissertation	Sept 2016 — Sep 2018

4. TITLE AND SUBTITLE

Numerical Simulation of High Energy Laser Propagation

5a. CONTRACT NUMBER

5b. GRANT NUMBER

5c. PROGRAM ELEMENT NUMBER

6. AUTHOR(S)

Dana F. Morrill

5d. PROJECT NUMBER

5e. TASK NUMBER

5f. WORK UNIT NUMBER

7. PERFORMING ORGANIZATION NAME(S) AND ADDRESS(ES)

Air Force Institute of Technology
Graduate School of Engineering and Management (AFIT/EN)
2950 Hobson Way
WPAFB OH 45433-7765

8. PERFORMING ORGANIZATION REPORT NUMBER

AFIT-ENC-DS-18-S-003

9. SPONSORING / MONITORING AGENCY NAME(S) AND ADDRESS(ES)

Department of Applied Mathematics
2950 Hobson Way
WPAFB OH 45433-7765
DSN 271-0690, COMM 937-255-3636
Email: dana.morrill@afit.edu

10. SPONSOR/MONITOR'S ACRONYM(S)

OSR, CDE

11. SPONSOR/MONITOR'S REPORT NUMBER(S)

12. DISTRIBUTION / AVAILABILITY STATEMENT

DISTRIBUTION STATEMENT A:
APPROVED FOR PUBLIC RELEASE; DISTRIBUTION UNLIMITED.

13. SUPPLEMENTARY NOTES

14. ABSTRACT High intensity lasers have many applications, such as in aerospace sciences wireless power transfer, and manufacturing. Fluid-laser interaction is important to predicting power at receiver, and other measures of laser beam quality. Typically the carrying medium of the laser is modeled statistically. This dissertation describes a novel method of coupling fluid evolution to beam propagation in free space. The coupled laser-fluid solver captures dynamic interaction of fluid temperature and beam intensity. Boundary conditions are compared in a novel study comparing the impact of three fluid boundary conditions on fluid simulation accuracy: periodic boundary conditions, finite box domain, and an open boundary condition. Scintillation is included in the final simulations. Scintillation is an important factor in laser beam quality. It is usually incorporated via phase-screens on the beam alone. A hybrid volumetric phase-screen model is developed to simulate laser-fluid interaction in the presence of small turbulence. The hybrid model is simulated and results of simulations, where scintillation is asymptotically incorporated into the coupled fluid-beam simulation, are presented.

15. SUBJECT TERMS

High Energy Laser, Fluid Dynamics, Open Boundary Conditions, Scintillation

16. SECURITY CLASSIFICATION OF:			17. LIMITATION OF ABSTRACT	18. NUMBER OF PAGES	19a. NAME OF RESPONSIBLE PERSON
a. REPORT	b. ABSTRACT	c. THIS PAGE			Dr. Benjamin F. Akers, AFIT/ENC
U	U	U	UU	92	19b. TELEPHONE NUMBER *(include area code)* (937) 255-3636, x4522; benjamin.akers@afit.edu